

Entropy stable numerical schemes for divergence diminishing Chew, Goldberger & Low equations for plasma flows

Chetan Singh^{a,*}, Harish Kumar^{a,b}, Deepak Bhoriya^c and Dinshaw S. Balsara^{d,e}

^aDepartment of Mathematics, Indian Institute of Technology Delhi, India

^bIITD-Abu Dhabi, Abu Dhabi, UAE

^cDepartment of Mathematics, BITS-Pilani, Pilani, Rajasthan, India

^dPhysics Department, University of Notre Dame, USA

^eACMS, University of Notre Dame, USA

ARTICLE INFO

Keywords:

CGL equations

GLM-CGL equations

GLM technique

Entropy stability

Divergence Cleaning

Entropy stable numerical schemes

ABSTRACT

Chew, Goldberger & Low (CGL) equations are a set of hyperbolic PDEs with non-conservative products used to model the plasma flows, when the assumption of *local thermodynamic equilibrium* is not valid, and the pressure tensor is assumed to be rotated by the magnetic field. This results in the pressure tensor, which is described by the two scalar components. As the magnetic field also evolves, controlling the divergence of the magnetic field is important. In this work, we consider the generalized Lagrange multiplier (GLM) technique for the CGL model. The resulting model is referred to as the GLM-CGL system. To make the system suitable for entropy-stable schemes, we reformulate the GLM-CGL system by treating some conservative terms as non-conservative. The resulting system has a non-conservative part that does not affect entropy evolution. We then propose entropy stable numerical methods for the GLM-CGL model. The numerical results for the GLM-CGL system are then compared with the CGL system without the GLM divergence diminishing approach to demonstrate that the GLM approach indeed leads to significant improvement in the magnetic field divergence diminishing.

1. Introduction

MHD has been proven remarkably successful in modelling a wide range of astrophysical phenomena (see [1, 2, 3]), including planetary magnetospheres (see [4, 5, 6]), heliosphere (see [7, 8, 9]), astrosphere (see [10, 11, 12]), turbulence (see [13, 14, 15]), and star formation (see [16, 17, 18]). MHD assumes *local thermodynamic equilibrium* for the plasma, which results in the isotropic pressure. However, for several applications, plasma is effectively collisionless; hence, the pressure cannot be assumed to be isotropic (see [19, 20, 21, 22, 23, 24, 25, 26, 27, 28, 29, 30, 31, 32, 33]). To overcome this, Chew, Goldberger and Low's equations were first introduced in [34]. The model assumes a gyrotropic description of pressure based on the two scalar pressure components (see [35, 36, 37, 33]).

The CGL equations are hyperbolic in nature and also contain non-conservative terms. Hence, the solutions can be discontinuous and weak solutions need to be considered. For numerical solutions, the presence of a non-conservative product leads to additional complications as the solution needs to consider a particular path (see [38, 39]). In practice, however, only linear paths are considered (see [33, 37]). In [40], the authors present WENO finite volume schemes for the model. Also, in [41], an entropy stable discretization is presented. In [42], the suitability of the CGL model for the heliospheric interface simulations is discussed. More recently, in [43], the eigenvalues and the right eigenvectors are presented for the model. These are then used to design HLL and HLLI approximated Riemann solvers and AFD-WENO schemes [44, 45].

For the two-dimensional simulations, the solutions of the CGL systems need to satisfy the divergence-free condition for the magnetic field. However, this is not guaranteed for numerical simulations even for MHD equations (see [46, 47, 48]). Hence, several strategies have been developed to overcome this difficulty (see [49, 50, 51, 52, 53, 54, 55, 56, 57, 58, 59, 60]). Furthermore, similar to the MHD, in CGL equations, the entropy evolution equation involves divergence of the magnetic field (see [41]). As the CGL system is hyperbolic, the entropy stability of the numerical

*Corresponding author.

✉ maz218518@iitd.ac.in (C. Singh); hkumar@iitd.ac.in (H. Kumar); dkbhoriya@gmail.com (D. Bhoriya); dbalsara@nd.edu (D.S. Balsara)

ORCID(s): 0009-0002-6822-8696 (C. Singh)

solution is also highly desirable. Hence, two key stability criteria for numerical schemes of the CGL equations are divergence-diminishing/free of the magnetic field and entropy stability. In this article, our aim is to address these issues using the following steps:

- Following the divergence diminishing strategy based on the Generalized Lagrange Multiplier (GLM) technique from [49, 51, 57, 58], we first propose the GLM-CGL system. We then analyze the entropy evolution of GLM-CGL model.
- Following [41], we reformulate the system by treating some conservative terms as non-conservative term, in such a way that the new non-conservative terms do not effect entropy production. We also symmetrize the conservative part by following [61, 41, 57, 58].
- To construct divergence diminishing entropy-stable schemes, we first design entropy-conservative numerical fluxes. Following [62], higher-order numerical diffusion operators are designed using a sign-preserving reconstruction and entropy-scaled eigenvectors. The derivatives in the non-conservative terms are approximated by appropriate central difference schemes. The whole spatial discretization is proved to entropy stable.
- For the numerical validation, several one and two-dimensional problems are considered. In all 2D test cases, we show that the GLM approach is beneficial in controlling the divergence error of the magnetic field evolution.

The rest of the article is organized as follows: In Section 2, we briefly describe the CGL equations. In Section 3, we propose, analyze and reformulate the GLM-CGL system. In Section 4, we present numerical discretization of the system. In Section 5, we discuss the fully discrete scheme by presenting time discretization. In Section 6, numerical tests are presented. Finally, we present concluding remarks in Section 7

2. CGL Model

The CGL model equations describing the plasma flow are given by (see [34, 35, 41, 40, 43]),

$$\frac{\partial}{\partial t} \begin{pmatrix} \rho \\ \rho \mathbf{v} \\ p_{\parallel} \\ e \\ \mathbf{B} \end{pmatrix} + \nabla \cdot \begin{pmatrix} \rho \mathbf{v} \\ \rho \mathbf{v} \mathbf{v} + p_{\perp} \mathbf{I} + (p_{\parallel} - p_{\perp}) \mathbf{b} \mathbf{b} - \left(\mathbf{B} \mathbf{B} - \frac{|\mathbf{B}|^2}{2} \mathbf{I} \right) \\ p_{\parallel} \mathbf{v} \\ \mathbf{v} \left(e + p_{\perp} + \frac{|\mathbf{B}|^2}{2} \right) + \mathbf{v} \cdot ((p_{\parallel} - p_{\perp}) \mathbf{b} \mathbf{b} - \mathbf{B} \mathbf{B}) \\ \mathbf{v} \mathbf{B} - \mathbf{B} \mathbf{v} \end{pmatrix} = \begin{pmatrix} 0 \\ \mathbf{0} \\ -2p_{\parallel} \mathbf{b} \cdot \nabla \mathbf{v} \cdot \mathbf{b} \\ 0 \\ \mathbf{0} \end{pmatrix}. \quad (1)$$

Here $\rho, \mathbf{v} = (v_x, v_y, v_z)^{\top}$ and $\mathbf{B} = (B_x, B_y, B_z)^{\top}$ denote density, velocity, and magnetic fields for the plasma flow. We denote unit magnetic vector as $\mathbf{b} = (b_x, b_y, b_z)^{\top} = \frac{\mathbf{B}}{|\mathbf{B}|}$. Using the unit vector, the symmetric pressure tensor \mathbf{P} is described as,

$$\mathbf{P} = p_{\parallel} \mathbf{b} \mathbf{b} + p_{\perp} (\mathbf{I} - \mathbf{b} \mathbf{b}).$$

Here p_{\parallel} is the parallel component and p_{\perp} is the perpendicular component of the pressure tensor. We also define the average scalar pressure as $p = \frac{2p_{\perp} + p_{\parallel}}{3}$. Using this, we close the system by defining total energy e as follows:

$$e = \frac{1}{2} (\rho |\mathbf{v}|^2 + |\mathbf{B}|^2 + 3p), \quad (2)$$

In addition, we need to impose divergence-free condition on the magnetic field, i.e. $\nabla \cdot \mathbf{B} = 0$.

3. GLM-CGL system

One possible approach to control the divergence error is based on the generalized Lagrange multiplier (GLM) method (see [49, 51, 59]). For the MHD equations, the first GLM-based reformulation was proposed in [51]. However, this formulation is not consistent with the entropy condition. In the same work, the authors also introduced an extended version of the GLM-based MHD reformulation, referred to as the *EGLM-MHD system*. Several authors [63, 59] have also adopted this formulation. Although this system is consistent with the entropy condition, the ninth component of

its entropy variable vanishes (see [57]), which makes this formulation unsuitable for the construction of entropy-stable schemes. Several other GLM-based divergence-diminishing approaches are considered in [64, 65, 66], but these are also not consistent with the entropy condition.

More recently, in [57], authors have proposed an entropy-consistent GLM reformulation of ideal MHD equations. We follow the same formulation to reformulate the CGL equations. The approach involves incorporating a Lagrange multiplier in the CGL system, namely, an auxiliary scalar field Ψ . In the rest of the article, we use red text to indicate the GLM terms.

Following [57], we introduce the GLM-variable Ψ , which evolves as,

$$\frac{\partial \Psi}{\partial t} + c_h(\nabla \cdot \mathbf{B}) + \mathbf{v} \cdot \nabla \Psi = 0, \quad (3)$$

where c_h is the hyperbolic divergence cleaning speed. The transport speed of Ψ is taken as the velocity \mathbf{v} , consistent with the velocity acting on \mathbf{B} in the (1e). The magnetic field equation is now modified to,

$$\frac{\partial \mathbf{B}}{\partial t} + \nabla \cdot (\mathbf{v}\mathbf{B} - \mathbf{B}\mathbf{v} + c_h\Psi\mathbf{I}) = 0. \quad (4)$$

Following [57], we note that the scalar $\Psi \rightarrow 0$ as $\nabla \cdot \mathbf{B} \rightarrow 0$. In addition, all the red-colored terms also vanish, allowing the model to return to the CGL equations (1). Thus, the GLM modification to the CGL system is consistent. We also modify the total energy (Eqn. (2)) to reflect the contribution of the GLM-variable Ψ and consider

$$E = e + \frac{1}{2}\Psi^2 = \frac{\rho|\mathbf{v}|^2}{2} + \frac{|\mathbf{B}|^2}{2} + \frac{3p}{2} + \frac{1}{2}\Psi^2, \quad (5)$$

as the new equation of state with the total energy equation as

$$\frac{\partial E}{\partial t} + \nabla \cdot \left[\mathbf{v} \left(e + p_{\perp} + \frac{|\mathbf{B}|^2}{2} \right) + \mathbf{v} \cdot ((p_{\parallel} - p_{\perp})\mathbf{b}\mathbf{b} - \mathbf{B}\mathbf{B}) + c_h\Psi\mathbf{B} \right] + \Psi\mathbf{v} \cdot \nabla \Psi = 0. \quad (6)$$

Finally, the **GLM-CGL system** is given by,

$$\frac{\partial}{\partial t} \begin{pmatrix} \rho \\ \rho\mathbf{v} \\ p_{\parallel} \\ E \\ \mathbf{B} \\ \Psi \end{pmatrix} + \nabla \cdot \left\{ \underbrace{\begin{pmatrix} \rho\mathbf{v} \\ \rho\mathbf{v}\mathbf{v} + p_{\perp}\mathbf{I} + (p_{\parallel} - p_{\perp})\mathbf{b}\mathbf{b} - \left(\mathbf{B}\mathbf{B} - \frac{|\mathbf{B}|^2}{2}\mathbf{I}\right) \\ p_{\parallel}\mathbf{v} \\ \mathbf{v} \left(e + p_{\perp} + \frac{|\mathbf{B}|^2}{2} \right) + \mathbf{v} \cdot ((p_{\parallel} - p_{\perp})\mathbf{b}\mathbf{b} - \mathbf{B}\mathbf{B}) \\ \mathbf{v}\mathbf{B} - \mathbf{B}\mathbf{v} \\ 0 \end{pmatrix}}_{\mathbf{f}_{cgl}} \right\} + \underbrace{\begin{pmatrix} 0 \\ 0 \\ 0 \\ c_h\Psi\mathbf{B} \\ c_h\Psi\mathbf{I} \\ c_h\mathbf{B} \end{pmatrix}}_{\mathbf{f}_{glm}} + \underbrace{\begin{pmatrix} 0 \\ 0 \\ 0 \\ \Psi\mathbf{v} \\ 0 \\ \mathbf{v} \end{pmatrix}}_{\eta_{glm}} \cdot (\nabla\Psi) = \underbrace{\begin{pmatrix} 0 \\ 0 \\ 0 \\ -2p_{\parallel}\mathbf{b} \cdot \nabla\mathbf{v} \cdot \mathbf{b} \\ 0 \\ 0 \end{pmatrix}}_{\eta_{cgl}} \quad (7)$$

The eigenvalues of the GLM-CGL system (7) are presented in Appendix A.

3.1. Entropy analysis

Let us denote $\mathbf{U} = (\rho, \rho\mathbf{v}, p_{\parallel}, E, \mathbf{B}, \Psi)^{\top}$ to be the conservative variable for the GLM-CGL system. Following [41], the entropy function is given by $\mathcal{E} = -\rho s$. Also, the entropy fluxes are given by $\mathbf{q}_x = v_x\mathcal{E}$ and $\mathbf{q}_y = v_y\mathcal{E}$ with,

$$s = \ln \left(\frac{\det \mathbf{P}}{\rho^5} \right) = \ln \left(\frac{p_{\parallel} p_{\perp}^2}{\rho^5} \right).$$

Then the entropy variable $\mathbf{V} = \frac{\partial \mathcal{E}}{\partial \mathbf{U}}$ for the GLM-CGL system (7) is,

$$\mathbf{V} = \left(5 - s - \beta_{\perp}|\mathbf{v}|^2, 2\beta_{\perp}\mathbf{v}, -\beta_{\parallel} + \beta_{\perp}, -2\beta_{\perp}, 2\beta_{\perp}\mathbf{B}, 2\beta_{\perp}\Psi \right)^{\top}, \quad (8)$$

where $\beta_{\perp} = \frac{\rho}{p_{\perp}}$ and $\beta_{\parallel} = \frac{\rho}{p_{\parallel}}$. We have the following lemma.

Lemma 3.1. *The smooth solutions of (7) satisfies*

$$\partial_t \mathcal{E} + \partial_x \mathbf{q}_x + \partial_y \mathbf{q}_y + \frac{2\rho(\mathbf{v} \cdot \mathbf{B})}{p_\perp} (\nabla \cdot \mathbf{B}) = 0, \quad (9)$$

which implies

$$\partial_t \mathcal{E} + \partial_x \mathbf{q}_x + \partial_y \mathbf{q}_y = 0, \quad (10)$$

if $\nabla \cdot \mathbf{B} = 0$.

Proof. We first note that

$$\begin{aligned} \mathbf{V}^\top (\nabla \cdot \mathbf{f}_{glm}) &= -2\beta_\perp (\nabla \cdot (c_h \Psi \mathbf{B})) + 2\beta_\perp \mathbf{B} (\nabla \cdot (c_h \Psi \mathbf{I})) + 2\beta_\perp \Psi (\nabla \cdot (c_h \mathbf{B})) \\ &= -2\beta_\perp (\nabla \cdot (c_h \Psi \mathbf{B})) + 2\beta_\perp \mathbf{B} (\nabla (c_h \Psi)) + 2\beta_\perp \Psi (\nabla \cdot (c_h \mathbf{B})) \\ &= -2\beta_\perp (\nabla \cdot (c_h \Psi \mathbf{B})) + 2\beta_\perp (\nabla \cdot (c_h \Psi \mathbf{B})) \\ &= 0. \end{aligned} \quad (11)$$

and

$$\mathbf{V}^\top \eta_{glm} = -2\beta_\perp (\Psi \mathbf{v} \cdot (\nabla \Psi)) + 2\beta_\perp \Psi (\mathbf{v} \cdot (\nabla \Psi)) = 0. \quad (12)$$

Furthermore, from [41], we have

$$\mathbf{V} \cdot (\partial_t \mathbf{U} + \nabla \cdot \mathbf{f}_{cgl} - \eta_{cgl}) = \partial_t \mathcal{E} + \partial_x \mathbf{q}_x + \partial_y \mathbf{q}_y + \frac{2\rho(\mathbf{v} \cdot \mathbf{B})}{p_\perp} (\nabla \cdot \mathbf{B}) = 0. \quad (13)$$

Combining (13), (11) and (12), we get

$$\mathbf{V}^\top \cdot (\partial_t \mathbf{U} + \nabla \cdot (\mathbf{f}_{cgl} + \mathbf{f}_{glm}) + \eta_{glm} - \eta_{cgl}) = \partial_t \mathcal{E} + \partial_x \mathbf{q}_x + \partial_y \mathbf{q}_y + \frac{2\rho(\mathbf{v} \cdot \mathbf{B})}{p_\perp} (\nabla \cdot \mathbf{B}) = 0. \quad (14)$$

□

We also note that the equality (10), turns into inequality

$$\partial_t \mathcal{E} + \partial_x \mathbf{q}_x + \partial_y \mathbf{q}_y \leq 0. \quad (15)$$

for the non-smooth solutions. Following [57, 58], the system (7) is consistent with the entropy inequality (15).

3.2. Reformulation of the GLM-CGL system

Following [67, 41], we reformulate the GLM-CGL system by considering some conservative terms as non-conservative products. We get,

$$\begin{aligned} \frac{\partial}{\partial t} \begin{pmatrix} \rho \\ \rho \mathbf{v} \\ p_\parallel \\ E \\ \mathbf{B} \\ \Psi \end{pmatrix} + \nabla \cdot \underbrace{\begin{pmatrix} \rho \mathbf{v} \\ \rho \mathbf{v} \mathbf{v} + p_\perp \mathbf{I} - \left(\mathbf{B} \mathbf{B} - \frac{|\mathbf{B}|^2}{2} \mathbf{I} \right) \\ p_\parallel \mathbf{v} \\ \mathbf{v} \left(e + p_\perp + \frac{|\mathbf{B}|^2}{2} \right) - \mathbf{v} \cdot (\mathbf{B} \mathbf{B}) + c_h \Psi \mathbf{B} \\ \mathbf{v} \mathbf{B} - \mathbf{B} \mathbf{v} + c_h \Psi \mathbf{I} \\ c_h \mathbf{B} \end{pmatrix}}_{\mathbf{f}_C} + \underbrace{\begin{pmatrix} 0 \\ 0 \\ 0 \\ \Psi \mathbf{v} \\ 0 \\ 0 \\ \mathbf{v} \end{pmatrix}}_{\eta_{glm}} \cdot (\nabla \Psi) + \underbrace{\begin{pmatrix} 0 \\ \nabla \cdot (p_\parallel - p_\perp) \mathbf{b} \mathbf{b} \\ 2p_\parallel \mathbf{b} \cdot \nabla \mathbf{v} \cdot \mathbf{b} \\ \nabla \cdot (\mathbf{v} \cdot ((p_\parallel - p_\perp) \mathbf{b} \mathbf{b})) \\ 0 \\ 0 \end{pmatrix}}_{\eta_{NC}} = \mathbf{0}. \end{aligned} \quad (16)$$

We note that the choice of non-conservative terms η_{NC} (blue colored) is such that $\mathbf{V}^\top \cdot \eta_{NC} = 0$ (see [41]). Also, from Eqn. (12), we already have $\mathbf{V}^\top \cdot \eta_{glm} = 0$. In two dimensions, we can now rewrite the GLM-CGL system (16) as follows:

$$\frac{\partial \mathbf{U}}{\partial t} + \frac{\partial \mathbf{f}_x}{\partial x} + \frac{\partial \mathbf{f}_y}{\partial y} + \Upsilon_x \frac{\partial \Psi}{\partial x} + \Upsilon_y \frac{\partial \Psi}{\partial y} + \mathbf{C}_x(\mathbf{U}) \frac{\partial \mathbf{U}}{\partial x} + \mathbf{C}_y(\mathbf{U}) \frac{\partial \mathbf{U}}{\partial y} = 0. \quad (17)$$

The flux functions are

$$\mathbf{f}_x = \begin{pmatrix} \rho v_x \\ \rho v_x^2 + p_\perp - \left(B_x^2 - \frac{|B|^2}{2} \right) \\ \rho v_x v_y - B_x B_y \\ \rho v_x v_z - B_x B_z \\ v_x \left(e + p_\perp + \frac{|B|^2}{2} \right) - B_x (\mathbf{B} \cdot \mathbf{v}) + c_h \Psi B_x \\ c_h \Psi \\ v_x B_y - v_y B_x \\ v_x B_z - v_z B_x \\ c_h B_x \end{pmatrix}, \quad \mathbf{f}_y = \begin{pmatrix} \rho v_y \\ \rho v_x v_y - B_x B_y \\ \rho v_y^2 + p_\perp - \left(B_y^2 - \frac{|B|^2}{2} \right) \\ \rho v_y v_z - B_y B_z \\ v_y \left(e + p_\perp + \frac{|B|^2}{2} \right) - B_y (\mathbf{B} \cdot \mathbf{v}) + c_h \Psi B_y \\ c_h \Psi \\ v_y B_x - v_x B_y \\ c_h \Psi \\ v_y B_z - v_z B_y \\ c_h B_y \end{pmatrix}.$$

The vectors Υ_x, Υ_y are defined as $\Upsilon_x = (0, \mathbf{0}, 0, \Psi v_x, \mathbf{0}, v_x)^\top$ and $\Upsilon_y = (0, \mathbf{0}, 0, \Psi v_y, \mathbf{0}, v_y)^\top$. The matrices $\mathbf{C}_x(\mathbf{U})$ and $\mathbf{C}_y(\mathbf{U})$ are given in Appendix B. The conservative fluxes \mathbf{f}_x and \mathbf{f}_y are similar to the GLM-MHD fluxes defined in [57]. Following [67, 41], we note that

$$\mathbf{q}_x'(\mathbf{U}) = \mathbf{V} \mathbf{f}_x'(\mathbf{U}), \quad \mathbf{q}_y'(\mathbf{U}) = \mathbf{V} \mathbf{f}_y'(\mathbf{U}), \quad (18)$$

and

$$\mathbf{V}^\top \Upsilon_x = \mathbf{V}^\top \Upsilon_y = 0, \quad (19)$$

Following [41], we also note that

$$\mathbf{V}^\top \mathbf{C}_x(\mathbf{U}) = \mathbf{V}^\top \mathbf{C}_y(\mathbf{U}) = 0. \quad (20)$$

Hence, for the system(17), following [67], the entropy-entropy flux pair is given by $(\mathcal{E}, \mathbf{q}_x, \mathbf{q}_y)$. Furthermore, we make following remark about the symmetrizability of the GLM-CGL system:

Remark 3.1. *Following [41], the GLM-CGL system is not symmetrizable.*

3.3. Symmetrization

To make equations suitable for the construction of entropy-stable numerical schemes, we now follow Godunov's process from [41, 68, 69, 61, 57, 70] for the conservative part. We consider,

$$\frac{\partial \mathbf{U}}{\partial t} + \frac{\partial \mathbf{f}_x}{\partial x} + \frac{\partial \mathbf{f}_y}{\partial y} = 0. \quad (21)$$

Following[41], we note that

$$\frac{\partial \mathbf{f}_x}{\partial \mathbf{V}} \neq \left(\frac{\partial \mathbf{f}_x}{\partial \mathbf{V}} \right)^\top \quad \text{and} \quad \frac{\partial \mathbf{f}_y}{\partial \mathbf{V}} \neq \left(\frac{\partial \mathbf{f}_y}{\partial \mathbf{V}} \right)^\top,$$

hence the conservative system is not symmetrizable, without assuming $\nabla \cdot \mathbf{B} = 0$.

Following [71, 68, 69, 61, 57, 70, 41], we rewrite the term $\frac{2\rho(\mathbf{v} \cdot \mathbf{B})}{\rho_\perp}$ using,

$$\Phi(\mathbf{V}) = \mathbf{V} \Phi'(\mathbf{V}) = \frac{2\rho(\mathbf{v} \cdot \mathbf{B})}{\rho_\perp}. \quad (22)$$

Differentiating,

$$\Phi'(\mathbf{V}) = [0, \mathbf{B}, 0, \mathbf{B} \cdot \mathbf{v}, \mathbf{v}, 0]. \quad (23)$$

We also define the entropy fluxes \mathbf{q}_x and \mathbf{q}_y

$$\mathbf{q}_x = \mathbf{V} \cdot \mathbf{f}_x + \Phi B_x - \mathcal{F}_x, \quad (24)$$

$$\mathbf{q}_y = \mathbf{V} \cdot \mathbf{f}_y + \Phi \mathbf{B}_y - \mathcal{F}_y, \quad (25)$$

with entropy potentials \mathcal{F}_x and \mathcal{F}_y

$$\mathcal{F}_x = \mathbf{V} \cdot \mathbf{f}_x + \Phi \mathbf{B}_x - \mathbf{q}_x = 2\rho v_x + \beta_\perp v_x |\mathbf{B}|^2 + 2c_h \beta_\perp \Psi \mathbf{B}_x, \quad (26)$$

$$\mathcal{F}_y = \mathbf{V} \cdot \mathbf{f}_y + \Phi \mathbf{B}_y - \mathbf{q}_y = 2\rho v_y + \beta_\perp v_y |\mathbf{B}|^2 + 2c_h \beta_\perp \Psi \mathbf{B}_y. \quad (27)$$

Finally, the Eqn. (21) is now symmetrizable if we consider the term $-\Phi'(\mathbf{V})^\top (\nabla \cdot \mathbf{B})$ on the right-hand side (red colored), which results in

$$\frac{\partial}{\partial t} \begin{pmatrix} \rho \\ \rho \mathbf{v} \\ p_\parallel \\ E \\ \mathbf{B} \\ \Psi \end{pmatrix} + \nabla \cdot \begin{pmatrix} \rho \mathbf{v} \\ \rho \mathbf{v} \mathbf{v} + p_\perp \mathbf{I} - \left(\mathbf{B} \mathbf{B} - \frac{|\mathbf{B}|^2}{2} \mathbf{I} \right) \\ p_\parallel \mathbf{v} \\ \mathbf{v} \left(e + p_\perp + \frac{|\mathbf{B}|^2}{2} \right) - \mathbf{v} \cdot (\mathbf{B} \mathbf{B}) + c_h \Psi \mathbf{B} \\ \mathbf{v} \mathbf{B} - \mathbf{B} \mathbf{v} + c_h \Psi \mathbf{I} \\ c_h \mathbf{B} \end{pmatrix} = - \begin{pmatrix} 0 \\ \mathbf{B} \\ 0 \\ \mathbf{v} \cdot \mathbf{B} \\ \mathbf{v} \\ 0 \end{pmatrix} (\nabla \cdot \mathbf{B}). \quad (28)$$

(a)
(b)
(c)
(d)
(e)
(f)

Together with GLM terms, we get,

$$\frac{\partial \mathbf{U}}{\partial t} + \frac{\partial \mathbf{f}_x}{\partial x} + \frac{\partial \mathbf{f}_y}{\partial y} + \Phi'(\mathbf{V})^\top (\nabla \cdot \mathbf{B}) + \Upsilon_x \frac{\partial \Psi}{\partial x} + \Upsilon_y \frac{\partial \Psi}{\partial y} = 0. \quad (29)$$

The system is similar to the GLM-MHD system derived in [57]. We further remark that with GLM terms, the system (29) is also symmetrizable. The x -direction eigenvalues of the system (29) are,

$$K_x = \{v_x, v_x, v_x \pm v_{ax}, v_x \pm c_h, v_x \pm c_f, v_x \pm c_s\}, \quad (30)$$

where

$$v_{ax}^2 = \frac{B_x^2}{\rho}, v_a^2 = \frac{B^2}{\rho}, a^2 = \frac{2p_\perp}{\rho}, \text{ and } c_{f,s}^2 = \frac{1}{2} \left[(v_a^2 + a^2) \pm \sqrt{(v_a^2 + a^2)^2 - 4v_{ax}^2 a^2} \right].$$

Similarly, for y -direction,

$$K_y = \{v_y, v_y, v_y \pm v_{ay}, v_y \pm c_h, v_y \pm c_f, v_y \pm c_s\} \quad (31)$$

where,

$$v_{ay}^2 = \frac{B_y^2}{\rho}, v_a^2 = \frac{B^2}{\rho}, a^2 = \frac{2p_\perp}{\rho}, \text{ and } c_{f,s}^2 = \frac{1}{2} \left[(v_a^2 + a^2) \pm \sqrt{(v_a^2 + a^2)^2 - 4v_{ay}^2 a^2} \right].$$

Following [68, 61, 41], we derive and present the entropy-scaled right eigenvectors for the system (29) in the x - and y -directions in Appendix C.

4. Semi-discrete numerical schemes

Combining the Godunov terms, GLM terms and additional non-conservative terms, we get,

$$\frac{\partial \mathbf{U}}{\partial t} + \frac{\partial \mathbf{f}_x}{\partial x} + \frac{\partial \mathbf{f}_y}{\partial y} + \Phi'(\mathbf{V})^\top (\nabla \cdot \mathbf{B}) + \Upsilon_x \frac{\partial \Psi}{\partial x} + \Upsilon_y \frac{\partial \Psi}{\partial y} + \mathbf{C}_x(\mathbf{U}) \frac{\partial \mathbf{U}}{\partial x} + \mathbf{C}_y(\mathbf{U}) \frac{\partial \mathbf{U}}{\partial y} = 0. \quad (32)$$

We will now propose entropy stable numerical schemes for these equations using finite difference method. Consider a uniform mesh for the computational domain with cells I_{ij} of size $\Delta x \times \Delta y$. We assume that the centers of the cell I_{ij} is denoted by (x_i, y_j) . The cell vertices are given by $(x_{i+\frac{1}{2}}, y_{j+\frac{1}{2}})$, with $x_{i+\frac{1}{2}} = \frac{x_i + x_{i+1}}{2}$ and $y_{j+\frac{1}{2}} = \frac{y_j + y_{j+1}}{2}$. A general

semi-discrete finite difference scheme for (32) on the uniform mesh is then given by

$$\begin{aligned} \frac{d}{dt} \mathbf{U}_{i,j} + \frac{\mathbf{f}_{x,i+\frac{1}{2},j} - \mathbf{f}_{x,i-\frac{1}{2},j}}{\Delta x} + \frac{\mathbf{f}_{y,i,j+\frac{1}{2}} - \mathbf{f}_{y,i,j-\frac{1}{2}}}{\Delta y} + \Phi'(\mathbf{V}_{i,j})^\top \left(\left(\frac{\partial \mathbf{B}_x}{\partial x} \right)_{i,j} + \left(\frac{\partial \mathbf{B}_y}{\partial y} \right)_{i,j} \right) \\ + \left((\Upsilon_x)_{i,j} \left(\frac{\partial \Psi}{\partial x} \right)_{i,j} + (\Upsilon_y)_{i,j} \left(\frac{\partial \Psi}{\partial y} \right)_{i,j} \right) + \mathbf{C}_x(\mathbf{U}_{i,j}) \left(\frac{\partial \mathbf{U}}{\partial x} \right)_{i,j} + \mathbf{C}_y(\mathbf{U}_{i,j}) \left(\frac{\partial \mathbf{U}}{\partial y} \right)_{i,j} = 0. \end{aligned} \quad (33)$$

Here, $\mathbf{f}_{x,i+\frac{1}{2},j}$ and $\mathbf{f}_{y,i,j+\frac{1}{2}}$ are the numerical fluxes, consistent with the continuous fluxes \mathbf{f}_x and \mathbf{f}_y in x - and y -directions, respectively. The derivatives in non-conservative terms are discretized with central difference of appropriate orders (see Appendix D). For the grid function $a_{i,j}$, let us introduce the notations

$$\llbracket a \rrbracket_{i+\frac{1}{2},j} = a_{i+1,j} - a_{i,j}, \quad \llbracket a \rrbracket_{i,j+\frac{1}{2}} = a_{i,j+1} - a_{i,j}$$

for the jumps across the cell interfaces and

$$\bar{a}_{i+\frac{1}{2},j} = \frac{a_{i+1,j} + a_{i,j}}{2}, \quad \bar{a}_{i,j+\frac{1}{2}} = \frac{a_{i,j+1} + a_{i,j}}{2},$$

for the averages across the cell boundaries.

4.1. Entropy conservative schemes

Following [72, 61, 41], to design entropy conservative scheme, we first need to satisfy the jump relations,

$$\llbracket \mathbf{V} \rrbracket_{i+\frac{1}{2},j} \cdot \tilde{\mathbf{f}}_{x,i+\frac{1}{2},j} = \llbracket \mathcal{F}_x \rrbracket_{i+\frac{1}{2},j} - \llbracket \Phi \rrbracket_{i+\frac{1}{2},j} \bar{\mathbf{B}}_{x,i+\frac{1}{2},j}, \quad (34)$$

$$\llbracket \mathbf{V} \rrbracket_{i,j+\frac{1}{2}} \cdot \tilde{\mathbf{f}}_{y,i,j+\frac{1}{2}} = \llbracket \mathcal{F}_y \rrbracket_{i,j+\frac{1}{2}} - \llbracket \Phi \rrbracket_{i,j+\frac{1}{2}} \bar{\mathbf{B}}_{y,i,j+\frac{1}{2}}. \quad (35)$$

Following [41], the entropy conservative flux

$$\tilde{\mathbf{f}}_x = [\tilde{f}_x^{(1)}, \tilde{f}_x^{(2)}, \tilde{f}_x^{(3)}, \tilde{f}_x^{(4)}, \tilde{f}_x^{(5)}, \tilde{f}_x^{(6)}, \tilde{f}_x^{(7)}, \tilde{f}_x^{(8)}, \tilde{f}_x^{(9)}, \tilde{f}_x^{(10)}]^\top,$$

is given by,

$$\begin{aligned} \tilde{f}_x^{(1)} &= \rho^{\ln} \bar{v}_x, \quad \tilde{f}_x^{(2)} = \frac{\bar{p}}{\beta_\perp} + \bar{v}_x \tilde{f}_x^{(1)} + \frac{1}{2} \overline{|\mathbf{B}|^2} - \bar{\mathbf{B}}_x \bar{\mathbf{B}}_x \\ \tilde{f}_x^{(3)} &= \bar{v}_y \tilde{f}_x^{(1)} - \bar{\mathbf{B}}_x \bar{\mathbf{B}}_y, \quad \tilde{f}_x^{(4)} = \bar{v}_z \tilde{f}_x^{(1)} - \bar{\mathbf{B}}_x \bar{\mathbf{B}}_z, \quad \tilde{f}_x^{(5)} = \frac{\tilde{f}_x^{(1)}}{\beta_\parallel^{\ln}}, \\ \tilde{f}_x^{(7)} &= c_h \frac{\overline{\Psi \beta_\perp}}{\bar{\beta}_\perp}, \quad \tilde{f}_x^{(8)} = \frac{1}{\bar{\beta}_\perp} \left(\overline{\beta_\perp v_x \bar{\mathbf{B}}_y} - \overline{\beta_\perp v_y \bar{\mathbf{B}}_x} \right), \quad \tilde{f}_x^{(9)} = \frac{1}{\bar{\beta}_\perp} \left(\overline{\beta_\perp v_x \bar{\mathbf{B}}_z} - \overline{\beta_\perp v_z \bar{\mathbf{B}}_x} \right), \\ \tilde{f}_x^{(10)} &= c_h \bar{\mathbf{B}}_x, \\ \tilde{f}_x^{(6)} &= \frac{1}{2} \left[\frac{2}{\beta_\perp^{\ln}} - \overline{|\mathbf{v}|^2} \right] \tilde{f}_x^{(1)} + \bar{v}_x \tilde{f}_x^{(2)} + \bar{v}_y \tilde{f}_x^{(3)} + \bar{v}_z \tilde{f}_x^{(4)} + \frac{\tilde{f}_x^{(5)}}{2} \\ &\quad + \bar{\mathbf{B}}_x \tilde{f}_x^{(7)} + \bar{\mathbf{B}}_y \tilde{f}_x^{(8)} + \bar{\mathbf{B}}_z \tilde{f}_x^{(9)} - \frac{1}{2} \bar{v}_x \overline{|\mathbf{B}|^2} + (\bar{v}_x \bar{\mathbf{B}}_x + \bar{v}_y \bar{\mathbf{B}}_y + \bar{v}_z \bar{\mathbf{B}}_z) \bar{\mathbf{B}}_x, \end{aligned}$$

where $a^{\ln} = \frac{\llbracket a \rrbracket}{\llbracket \ln a \rrbracket}$ denotes the logarithmic average for the scalar grid function a . We have ignored the spatial indexing to simplify the notations. Similarly, $\tilde{\mathbf{f}}_y$, the entropy conservative flux in y -direction can be obtained.

Therefore, the numerical scheme (33) with entropy conservative numerical fluxes $\tilde{\mathbf{f}}_{x,i+\frac{1}{2},j} = \tilde{\mathbf{f}}_x(\mathbf{U}_{i,j}, \mathbf{U}_{i+1,j})$ and $\tilde{\mathbf{f}}_{y,i,j+\frac{1}{2}} = \tilde{\mathbf{f}}_y(\mathbf{U}_{i,j}, \mathbf{U}_{i,j+1})$ is entropy conservative and second-order accurate. We have highlighted the additional terms in red, compared to the numerical flux in [41]. These terms arise due to the GLM formulation.

To obtain the higher-order entropy conservative numerical schemes, we follow [73] to construct $2p^{th}$ -order accurate fluxes using second-order fluxes for any positive integer p . In particular for ($p = 2$), the 4^{th} -order x -directional entropy conservative flux $\tilde{\mathbf{f}}_{x,i+\frac{1}{2},j}^4$ is given below

$$\tilde{\mathbf{f}}_{x,i+\frac{1}{2},j}^4 = \frac{4}{3}\tilde{\mathbf{f}}_x(\mathbf{U}_{i,j}, \mathbf{U}_{i+1,j}) - \frac{1}{6}\left(\tilde{\mathbf{f}}_x(\mathbf{U}_{i-1,j}, \mathbf{U}_{i+1,j}) + \tilde{\mathbf{f}}_x(\mathbf{U}_{i,j}, \mathbf{U}_{i+2,j})\right). \quad (36)$$

Similarly, we can derive the fourth-order entropy conservative flux $\tilde{\mathbf{f}}_{y,i,j+\frac{1}{2}}^4$ in y -direction. Again, following [41], the numerical scheme (33) with fourth order numerical fluxes described above and fourth order discretization of derivatives of the non-conservative derivative results in a fourth order entropy conservative scheme.

4.2. Entropy stable schemes

To design entropy-stable numerical schemes, following [72], we modify the entropy conservative numerical fluxes as follows

$$\hat{\mathbf{f}}_{x,i+\frac{1}{2},j} = \tilde{\mathbf{f}}_{x,i+\frac{1}{2},j} - \frac{1}{2}\mathbf{D}_{x,i+\frac{1}{2},j}\llbracket\mathbf{V}\rrbracket_{i+\frac{1}{2},j}, \quad \hat{\mathbf{f}}_{y,i,j+\frac{1}{2}} = \tilde{\mathbf{f}}_{y,i,j+\frac{1}{2}} - \frac{1}{2}\mathbf{D}_{y,i,j+\frac{1}{2}}\llbracket\mathbf{V}\rrbracket_{i,j+\frac{1}{2}}, \quad (37)$$

where $\mathbf{D}_{x,i+\frac{1}{2},j}$ and $\mathbf{D}_{y,i,j+\frac{1}{2}}$ are symmetric positive definite matrices. We use Rusanov's type diffusion matrices, given by

$$\mathbf{D}_{x,i+\frac{1}{2},j} = \tilde{\mathbf{R}}_{x,i+\frac{1}{2},j}\Lambda_{x,i+\frac{1}{2},j}\tilde{\mathbf{R}}_{x,i+\frac{1}{2},j}^T \quad \text{and} \quad \mathbf{D}_{y,i,j+\frac{1}{2}} = \tilde{\mathbf{R}}_{y,i,j+\frac{1}{2}}\Lambda_{y,i,j+\frac{1}{2}}\tilde{\mathbf{R}}_{y,i,j+\frac{1}{2}}^T, \quad (38)$$

where, $\tilde{\mathbf{R}}_d$, $d \in \{x, y\}$ are the matrices of entropy-scaled right eigenvectors derived in Appendix C, following [68, 41]. Also, Λ_d are,

$$\Lambda_d = \left(\max_{1 \leq k \leq 10} |\lambda_d^k| \right) \mathbf{I}_{10 \times 10},$$

where $\{\lambda_d^k : 1 \leq k \leq 10\}$ are given by (30) and (31) for the system (29) in x and y -directions, respectively. To achieve higher order, we follow [74], to reconstruct *scaled entropy variables*

$$\mathcal{W}_{x,i,j}^\pm = \tilde{\mathbf{R}}_{x,i\pm\frac{1}{2},j}^T \mathbf{V}_{i,j},$$

using the ENO procedure, to get the reconstructed polynomials $\mathcal{P}_{x,i,j}^\pm(x_{i\pm\frac{1}{2}})$ of appropriate order. The ENO procedure has the *sign-preserving property* [62], which ensures the entropy stability. For the second order. We use the MinMod limiter, which also has sign-preserving property. The reconstructed values of scaled entropy variables are given by

$$\hat{\mathcal{W}}_{x,i,j}^\pm = \mathcal{P}_{x,i,j}^\pm(x_{i\pm\frac{1}{2}}).$$

Using these, we define the reconstructed scaled variables as

$$\hat{\mathbf{V}}_{x,i,j}^\pm = \left\{ \tilde{\mathbf{R}}_{x,i\pm\frac{1}{2},j}^T \right\}^{(-1)} \hat{\mathcal{W}}_{x,i,j}^\pm.$$

Finally, we denote,

$$\hat{\mathbf{f}}_{x,i+\frac{1}{2},j}^k = \tilde{\mathbf{f}}_{x,i+\frac{1}{2},j}^{2p} - \frac{1}{2}\mathbf{D}_{x,i+\frac{1}{2},j}\llbracket\hat{\mathbf{V}}\rrbracket_{x,i+\frac{1}{2},j}^k. \quad (39)$$

where

$$\llbracket\hat{\mathbf{V}}\rrbracket_{x,i+\frac{1}{2},j}^k = \hat{\mathbf{V}}_{x,i+1,j}^- - \hat{\mathbf{V}}_{x,i,j}^+.$$

Similarly, we get,

$$\hat{\mathbf{f}}_{y,i,j+\frac{1}{2}}^k = \tilde{\mathbf{f}}_{y,i,j+\frac{1}{2}}^{2p} - \frac{1}{2}\mathbf{D}_{y,i,j+\frac{1}{2}}\llbracket\hat{\mathbf{V}}\rrbracket_{y,i,j+\frac{1}{2}}^k. \quad (40)$$

An appropriate value of p is considered for the different orders of schemes. For the scheme (33), we now get,

Theorem 4.1 (see [41]). *The scheme using entropy stable fluxes (39),(40) and with second-order (for $k = 2$) and fourth-order (for $k = 3, 4$) central difference approximations for $\left(\frac{\partial B_x}{\partial x}\right)_{i,j}$, $\left(\frac{\partial B_y}{\partial y}\right)_{i,j}$, $\left(\frac{\partial \Psi}{\partial x}\right)_{i,j}$, $\left(\frac{\partial \Psi}{\partial y}\right)_{i,j}$, $\left(\frac{\partial U}{\partial x}\right)_{i,j}$, and $\left(\frac{\partial U}{\partial y}\right)_{i,j}$ is k^{th} -order accurate and entropy stable (where $k = 2, 3, 4$), i.e. it satisfies*

$$\frac{d}{dt} \mathcal{E}(U_{i,j}) + \frac{1}{\Delta x} \left(\hat{q}_{x,i+\frac{1}{2},j}^k - \hat{q}_{x,i-\frac{1}{2},j}^k \right) + \frac{1}{\Delta y} \left(\hat{q}_{y,i,j+\frac{1}{2}}^k - \hat{q}_{y,i,j-\frac{1}{2}}^k \right) \leq 0, \quad (41)$$

where \hat{q}_x^k and \hat{q}_y^k are given by

$$\hat{q}_{x,i+\frac{1}{2},j}^k = \tilde{q}_{x,i+\frac{1}{2},j}^{2p} - \frac{1}{2} \bar{\mathbf{V}}_{i+\frac{1}{2},j}^\top \mathbf{D}_{x,i+\frac{1}{2},j} \llbracket \hat{\mathbf{V}} \rrbracket_{x,i+\frac{1}{2},j}^k$$

and

$$\hat{q}_{y,i,j+\frac{1}{2}}^k = \tilde{q}_{y,i,j+\frac{1}{2}}^{2p} - \frac{1}{2} \bar{\mathbf{V}}_{i,j+\frac{1}{2}}^\top \mathbf{D}_{y,i,j+\frac{1}{2}} \llbracket \hat{\mathbf{V}} \rrbracket_{y,i,j+\frac{1}{2}}^k.$$

To compute the isotropic limit solutions, we consider the following source term,

$$\mathbf{S} = \left\{ \mathbf{0}_{1 \times 4}, \frac{p_\perp - p_\parallel}{\tau}, \mathbf{0}_{1 \times 4}, \mathbf{0} \right\}^\top \quad (42)$$

This source relaxes the solution to the isotropic limit. Here, τ is a constant.

5. Time discretization

Let U^n be the solution at $t = t^n$ and $\Delta t = t^{n+1} - t^n$. Then the scheme (33) including the source term $\mathbf{S}(U_{i,j})$, can be represented as,

$$\frac{d}{dt} U_{i,j}(t) = \mathcal{L}_{i,j}(U(t)) + \mathbf{S}(U_{i,j}(t)), \quad (43)$$

where,

$$\begin{aligned} \mathcal{L}_{i,j}(U(t)) = & - \frac{\hat{\mathbf{f}}_{x,i+\frac{1}{2},j}^k - \hat{\mathbf{f}}_{x,i-\frac{1}{2},j}^k}{\Delta x} - \frac{\hat{\mathbf{f}}_{y,i,j+\frac{1}{2}}^k - \hat{\mathbf{f}}_{y,i,j-\frac{1}{2}}^k}{\Delta y} - \Phi'(\mathbf{V}_{i,j})^\top \left(\left(\frac{\partial B_x}{\partial x} \right)_{i,j} + \left(\frac{\partial B_y}{\partial y} \right)_{i,j} \right) \\ & - \left((\Upsilon_x)_{i,j} \left(\frac{\partial \Psi}{\partial x} \right)_{i,j} + (\Upsilon_y)_{i,j} \left(\frac{\partial \Psi}{\partial y} \right)_{i,j} \right) - \mathbf{C}_x(U_{i,j}) \left(\frac{\partial U}{\partial x} \right)_{i,j} + \mathbf{C}_y(U_{i,j}) \left(\frac{\partial U}{\partial y} \right)_{i,j}. \end{aligned}$$

When we compute the anisotropic (CGL) solutions, we do not consider the source term \mathbf{S} . So, we use the explicit SSP-RK methods from [75]. These schemes are summarized as follows:

- **O2_{exp}^{es}** : We take $p = 1$ for the entropy conservative numerical flux. For the diffusion operator, we use *MinMod*-based sign-preserving reconstruction. The derivatives $\left(\frac{\partial B_x}{\partial x}\right)_{i,j}$, $\left(\frac{\partial B_y}{\partial y}\right)_{i,j}$, $\left(\frac{\partial \Psi}{\partial x}\right)_{i,j}$, $\left(\frac{\partial \Psi}{\partial y}\right)_{i,j}$, $\left(\frac{\partial U}{\partial x}\right)_{i,j}$, and $\left(\frac{\partial U}{\partial y}\right)_{i,j}$ are approximated by second order central difference. For the time update, we use the second-order SSP-RK method.
- **O3_{exp}^{es}** : Here, we take $p = 2$ for the entropy conservative part. For the diffusion operator, we use third-order ENO-based sign-preserving reconstruction. The derivatives $\left(\frac{\partial B_x}{\partial x}\right)_{i,j}$, $\left(\frac{\partial B_y}{\partial y}\right)_{i,j}$, $\left(\frac{\partial \Psi}{\partial x}\right)_{i,j}$, $\left(\frac{\partial \Psi}{\partial y}\right)_{i,j}$, $\left(\frac{\partial U}{\partial x}\right)_{i,j}$, and $\left(\frac{\partial U}{\partial y}\right)_{i,j}$, are approximated using fourth-order central difference. For the time update, we use the third-order SSP-RK method.

- $\mathbf{O4}_{\text{exp}}^{\text{es}}$: Here, we take $p = 2$ for the entropy conservative part.. For the diffusion operator, we use fourth-order ENO-based sign-preserving reconstruction. The derivatives $\left(\frac{\partial B_x}{\partial x}\right)_{i,j}$, $\left(\frac{\partial B_y}{\partial y}\right)_{i,j}$, $\left(\frac{\partial \Psi}{\partial x}\right)_{i,j}$, $\left(\frac{\partial \Psi}{\partial y}\right)_{i,j}$, $\left(\frac{\partial \mathbf{U}}{\partial x}\right)_{i,j}$, and $\left(\frac{\partial \mathbf{U}}{\partial y}\right)_{i,j}$, are approximated using fourth-order central difference. For the time update, we use the fourth-order SSP-RK method.

To compute *isotropic* (MHD) solutions, we consider the source terms (42). As lower values of τ make the system stiff, we use ARK-IMEX schemes [76, 77], where we treat $\mathcal{L}_{i,j}(\mathbf{U}(t))$ explicitly and $\mathbf{S}(\mathbf{U}_{i,j}(t))$ implicitly. We summarize these schemes as follows:

- $\mathbf{O2}_{\text{imex}}^{\text{es}}$: The discretization of $\mathcal{L}_{i,j}(\mathbf{U}(t))$ is same as in the case of $\mathbf{O2}_{\text{exp}}^{\text{es}}$. For the ARK-IMEX time update, we follow, [76] and consider second-order scheme which is L-stable, where $\mathbf{S}(\mathbf{U}_{i,j}(t))$ is treated implicitly.
- $\mathbf{O3}_{\text{imex}}^{\text{es}}$: The discretization of $\mathcal{L}_{i,j}(\mathbf{U}(t))$ is same as in $\mathbf{O3}_{\text{exp}}^{\text{es}}$. The source term $\mathbf{S}(\mathbf{U}_{i,j}(t))$ is treated implicitly, in the third-order ARK-IMEX scheme from [77].
- $\mathbf{O4}_{\text{imex}}^{\text{es}}$: The term $\mathcal{L}_{i,j}(\mathbf{U}(t))$ is discretized as in $\mathbf{O4}_{\text{exp}}^{\text{es}}$. We use fourth order ARK-IMEX scheme from [77], where we treat $\mathbf{S}(\mathbf{U}_{i,j}(t))$, implicitly.

6. Numerical results

In this section, we present the numerical results for the various one and two-dimensional test cases. Following [57, 58], we take the hyperbolic divergence cleaning speed

$$c_h = \alpha \left(\max \{ \Lambda_x - \{v_x + c_h, v_x - c_h\} \} \right), \quad \alpha \in (0, 1],$$

for the one-dimensional cases. For the two-dimensional cases, we take

$$c_h = \alpha \left(\max \{ \Lambda_x - \{v_x + c_h, v_x - c_h\}, \Lambda_y - \{v_y + c_h, v_y - c_h\} \} \right), \quad \alpha \in (0, 1].$$

We take $\alpha = 1.0$. The time-step size is estimated as

$$\Delta t = \frac{\text{CFL}}{\max_{i,j} \left(\frac{\lambda_x(\mathbf{U}_{i,j})}{\Delta x} + \frac{\lambda_y(\mathbf{U}_{i,j})}{\Delta y} \right)},$$

where

$$\lambda_x = \max_{\lambda \in \Lambda_x} |\lambda| \quad \text{and} \quad \lambda_y = \max_{\lambda \in \Lambda_y} |\lambda|.$$

We take $\text{CFL} = 0.4$ for all test cases. For the source terms, we take $\tau = 10^{-5}$. We call these solutions as *isotropic GLM-CGL* solutions. The solution without the source terms is termed as *GLM-CGL* solutions. If no GLM divergence diminishing is used, the solution without source terms is called *CGL* solution. Similarly, solutions with source terms, but no GLM divergence diminishing, are termed as *isotropic CGL* solutions. To compare the isotropic solutions and MHD solutions, we have computed MHD solutions. For that, we use second-order finite volume methods with MinMod-based reconstruction. We use the Rusanov solver for the numerical flux. For 1D, we use 10000 cells. For 2D, we use highly refined mesh of 1000×1000 cells.

For two-dimensional test cases, to show the effect of GLM terms on the simulations, we calculate the divergence errors for the magnetic field in L_1 -norm,

$$\|\nabla \cdot \mathbf{B}\|_1 = \frac{1}{N_x N_y} \sum_{i=1}^{N_x} \sum_{j=1}^{N_y} |(\nabla \cdot \mathbf{B})_{i,j}|,$$

and L_2 -norm,

$$\|\nabla \cdot \mathbf{B}\|_2 = \left[\frac{1}{N_x N_y} \sum_{i=1}^{N_x} \sum_{j=1}^{N_y} |(\nabla \cdot \mathbf{B})_{i,j}|^2 \right]^{\frac{1}{2}}.$$

Number of cells	$\mathbf{O2}_{\text{exp}}^{\text{es}}$		$\mathbf{O3}_{\text{exp}}^{\text{es}}$		$\mathbf{O4}_{\text{exp}}^{\text{es}}$	
	L_1 error	Order	L_1 error	Order	L_1 error	Order
12	4.86E-02	–	7.14E-03	–	1.98E-03	–
24	1.51E-02	1.688145847	9.35E-04	2.932342894	2.09E-04	3.241997756
48	6.67E-03	1.176375673	1.18E-04	2.986256366	1.61E-05	3.704200874
96	1.93E-03	1.789540351	1.48E-05	2.996555203	1.16E-06	3.793435746
192	5.32E-04	1.85985482	1.85E-06	2.999133857	8.02E-08	3.852029024
384	1.46E-04	1.863664412	2.31E-07	2.999760591	5.40E-09	3.892946082

Table 1
One-dimensional accuracy test: L_1 errors and order of accuracy for ρ .

Here N_x and N_y denote the number of grid cells in the x and y -directions. The discrete divergence error $(\nabla \cdot \mathbf{B})_{i,j}$ is evaluated using

$$(\nabla \cdot \mathbf{B})_{i,j} = \frac{B_{x,i+1,j} - B_{x,i-1,j}}{2\Delta x} + \frac{B_{y,i,j+1} - B_{y,i,j-1}}{2\Delta y}.$$

6.1. One-dimensional accuracy test

In this test case, we demonstrate the accuracy of the proposed numerical schemes for the GLM-CGL system. We adapt the MHD test problem from [78]. The computational domain is $[0, 2\pi]$, with periodic boundary conditions. The initial data is given as,

$$\begin{aligned} \rho(x, 0) &= 1 + 0.2 \sin x, \\ (\mathbf{v}, p_{\parallel}, p_{\perp}, \mathbf{B}, \Psi) &= (1, 0, 0, 2, 2, 0.5, 1.0, 1.5, 0). \end{aligned}$$

We do not consider the source term in this test case. The simulations are performed till time $t = 1.3$. The exact solution of the problem is $\rho(x, t) = 1 + 0.2 \sin(x - t)$, which is the advection of the density profile with unit velocity in the x -direction. In Table (1), we have presented the L_1 -errors and numerical order of convergence for density variables, using $\mathbf{O2}_{\text{exp}}^{\text{es}}$, $\mathbf{O3}_{\text{exp}}^{\text{es}}$ and $\mathbf{O4}_{\text{exp}}^{\text{es}}$ schemes for the GLM-CGL system. All the schemes have achieved the predicted order.

6.2. One-dimensional artificial non-zero magnetic field divergence test

Following [57], in this test, we consider an initial condition with non-zero divergence. As numerically, the initial conditions might not have a non-zero divergence of the magnetic field (poorly chosen initial conditions), we want to present the GLM-CGL framework to demonstrate the ability of the method to deal with such a situation. The computational domain is taken to $[-1, 1]$ with Neumann boundary conditions. The magnetic field component B_x is given by,

$$B_x = \begin{cases} 0.0, & \text{if } x \leq -0.8 \\ -2(x + 0.8), & \text{if } -0.8 < x \leq -0.6 \\ \exp\left(-\frac{(x/0.11)^2}{2}\right), & \text{if } -0.6 < x \leq 0.6 \\ 0.5, & \text{otherwise.} \end{cases}$$

The rest of the variables are taken to be constants and given by,

$$(\rho, \mathbf{v}, p_{\parallel}, p_{\perp}, B_y, B_z, \Psi) = (1, 0, 0, 0, 1, 1, 0, 0, 0).$$

To demonstrate the effect of GLM-based formulation, we have compared the GLM-CGL formulation with the CGL equations without GLM. The numerical results for $\mathbf{O2}_{\text{exp}}^{\text{es}}$, $\mathbf{O3}_{\text{exp}}^{\text{es}}$ and $\mathbf{O4}_{\text{exp}}^{\text{es}}$ schemes for both the formulations are presented in Figure (1) at time $t = 0, 1, 2$ and 3 .

For the CGL equation without GLM, we observe that $\mathbf{O2}_{\text{exp}}^{\text{es}}$, $\mathbf{O3}_{\text{exp}}^{\text{es}}$ and $\mathbf{O4}_{\text{exp}}^{\text{es}}$ schemes (Figures (1(a)), (1(b)) and (1(c))) preserve the initial profile of the x -magnetic field component (B_x). So, the divergence of the initial profile is not diminished. We observe only slight diffusion in the B_x profile over time.

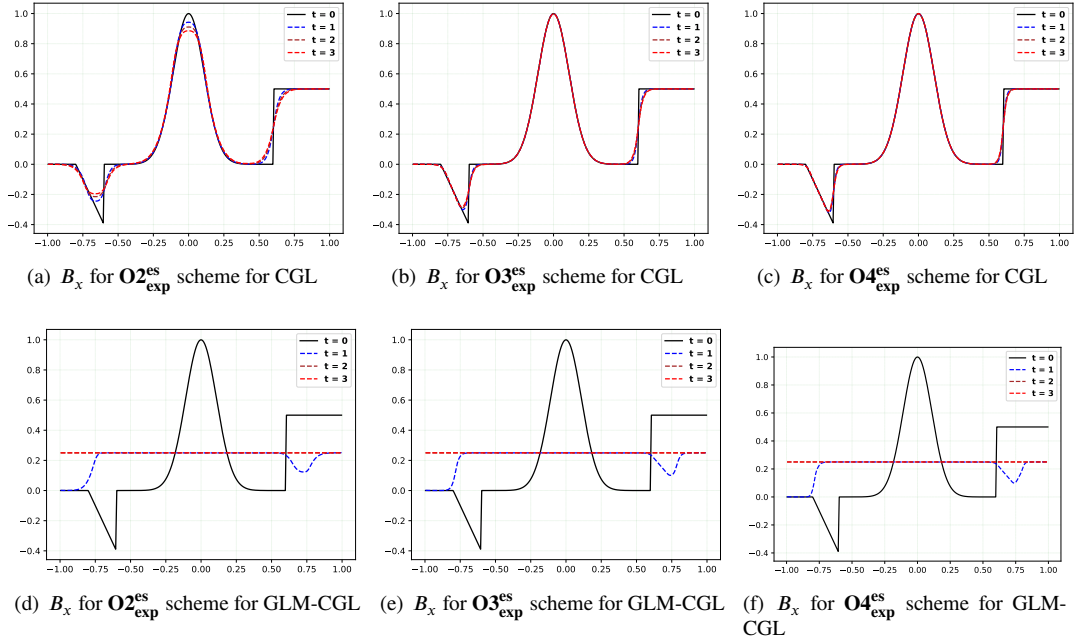


Figure 1: One-dimensional artificial non-zero magnetic field divergence test: Plots of magnetic field evolution for $\mathbf{O2}_{\text{exp}}^{\text{es}}$, $\mathbf{O3}_{\text{exp}}^{\text{es}}$ and $\mathbf{O4}_{\text{exp}}^{\text{es}}$ schemes for CGL and GLM-CGL at four different time steps.

In Figures (1(d)), (1(e)) and (1(f)), we have plotted the magnetic field evolution B_x for the $\mathbf{O2}_{\text{exp}}^{\text{es}}$, $\mathbf{O3}_{\text{exp}}^{\text{es}}$ and $\mathbf{O4}_{\text{exp}}^{\text{es}}$ schemes for GLM-CGL. In this case, we observe that as time increases, the divergence of the magnetic field decreases and becomes zero at $t = 3$. This demonstrates that the GLM-CGL formulation deals with the divergence effectively, even in a one-dimensional case. We also observe that all the numerical schemes behave similarly, with higher-order schemes being less diffusive. Furthermore, the results are comparable to those obtained in [57] for MHD equations.

6.3. Brio-Wu shock tube problem

In this test, we generalize the Brio-Wu shock tube test case for MHD equations [79]. The test was also considered in [41, 43]. Following [41], we take the computational domain to be $[-1, 1]$ with Neumann boundary conditions. The initial conditions are:

$$(\rho, \mathbf{v}, p_{\parallel}, p_{\perp}, B_x, B_y, B_z, \Psi) = \begin{cases} (1, 0, 0, 0, 1, 1, 0.75, 1, 0, 0), & \text{if } x \leq 0 \\ (0.125, 0, 0, 0, 0, 0.1, 0.1, 0.75, -1, 0, 0), & \text{otherwise} \end{cases}$$

In Figure (2), we present the numerical results at time $t = 0.2$ for CGL and GLM-CGL formulations. We also consider the isotropic CGL and isotropic GLM-CGL by considering the source term and using IMEX schemes $\mathbf{O2}_{\text{imex}}^{\text{es}}$, $\mathbf{O3}_{\text{imex}}^{\text{es}}$ and $\mathbf{O4}_{\text{imex}}^{\text{es}}$. The simulations use 2000 cells. We have also compared MHD and isotropic solutions. We have plotted profiles of density, p_{\parallel} and p_{\perp} for all the test cases.

For the CGL and GLM-CGL, we observe that all schemes successfully resolve the waves. We observe small-scale oscillations (similar to those in [41]), but they decrease with further refinements. We also observe that the GLM-CGL solutions are slightly more diffusive than the CGL solutions for the same order of scheme.

For the isotropic cases, we note that both p_{\parallel} and p_{\perp} have the same profile (which matches the MHD pressure profile), as expected. Furthermore, the density profile matches the MHD density profile. Furthermore, we again see that isotropic GLM-CGL solutions are slightly more diffusive than the isotropic CGL solution. In all the cases, we also observe that higher-order schemes are more accurate.

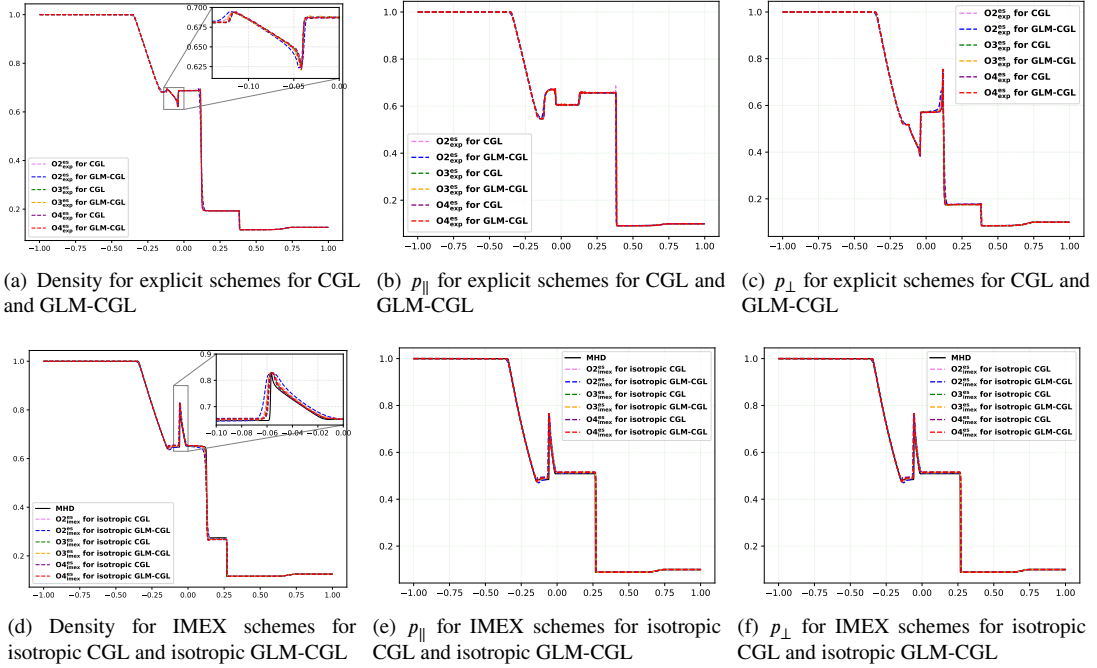


Figure 2: Brio-Wu shock tube problem: Plots of density, parallel and perpendicular pressure components for explicit schemes and IMEX schemes using 2000 cells at final time $t = 0.2$.

Number of cells	$\mathbf{O2}_{exp}^{es}$		$\mathbf{O3}_{exp}^{es}$		$\mathbf{O4}_{exp}^{es}$	
	L_1 error	Order	L_1 error	Order	L_1 error	Order
24×24	2.22E-02	—	1.47E-03	—	3.29E-04	—
48×48	9.66E-03	1.197102245	1.88E-04	2.97345722	2.60E-05	3.665723172
96×96	3.00E-03	1.685415758	2.35E-05	2.995912704	1.87E-06	3.79493394
192×192	8.43E-04	1.834041352	2.94E-06	2.999439213	1.30E-07	3.845890159
384×384	2.32E-04	1.858969497	3.68E-07	2.999783442	8.78E-09	3.888987053

Table 2

Two-dimensional accuracy test: L_1 errors and order of accuracy for ρ .

6.4. Two-dimensional accuracy test

For the two-dimensional accuracy test, we generalize the one-dimensional accuracy test in Section 6.1 to two dimensions for the GLM-CGL system. We consider the computational domain $[0, 2\pi] \times [0, 2\pi]$ with periodic boundary conditions. The initial conditions are given below,

$$\rho(x, y, 0) = 1 + 0.2 \sin(x + y),$$

$$(\mathbf{v}, p_{\parallel}, p_{\perp}, \mathbf{B}, \Psi) = (0.5, 0.5, 0, 2, 2, 0.5, 1.0, 1.5, 0).$$

The exact solution is then given by $\rho(x, y, t) = 1 + 0.2 \sin(x + y - t)$. For the $\mathbf{O2}_{exp}^{es}$, $\mathbf{O3}_{exp}^{es}$ and $\mathbf{O4}_{exp}^{es}$ schemes with GLM, the L_1 -errors of the density are shown in Table(2) at the final time of $t = 1.3$. We note that all the schemes converge with the theoretically predicted order of accuracy.

6.5. Two-dimensional Circularly polarized Alfvén waves

To test the accuracy of the magnetic field components, in this test we consider the generalization of the two-dimensional MHD circularly polarized Alfvén waves problem, which was introduced in [80], for the GLM-CGL system. We consider the computational domain is $\left[0, \frac{1}{\cos \alpha}\right] \times \left[0, \frac{1}{\sin \alpha}\right]$, with periodic boundary conditions. The initial condition

Number of cells	$\mathbf{O2}_{\text{exp}}^{\text{es}}$		$\mathbf{O3}_{\text{exp}}^{\text{es}}$		$\mathbf{O4}_{\text{exp}}^{\text{es}}$	
	L_1 error	Order	L_1 error	Order	L_1 error	Order
32×32	2.53E-02	–	1.25E-03	–	2.92E-04	–
64×64	8.06E-03	1.649122178	1.57E-04	2.997015955	2.39E-05	3.606907328
128×128	3.49E-03	1.208907716	2.01E-05	2.964144554	1.69E-06	3.825756677
256×256	9.84E-04	1.824933152	2.55E-06	2.978762804	1.13E-07	3.898604125
512×512	2.75E-04	1.840806962	3.26E-07	2.965870547	6.36E-09	4.153053838

Table 3

Two-dimensional Circularly polarized Alfvén waves: L_1 errors and order of accuracy for B_y .

is given as

$$\begin{aligned}
 (\rho, p_{\parallel}, p_{\perp}, \Psi) &= (1, 0.1, 0.1, 0), \\
 \mathbf{v} &= (-v_{\perp} \sin \alpha, v_{\perp} \cos \alpha, 0.1 \cos(2\pi x_{\parallel})), \\
 \mathbf{B} &= (B_{\parallel} \cos \alpha - B_{\perp} \sin \alpha, B_{\parallel} \sin \alpha + B_{\perp} \cos \alpha, v_z),
 \end{aligned}$$

where $B_{\parallel} = 1$, $B_{\perp} = v_{\perp} = 0.1 \sin(2\pi x_{\parallel})$ and $x_{\parallel} = x \cos \alpha + y \sin \alpha$. Circularly polarized alfvén wave have a unit wavelength in the direction of the x -axis and propagate at an angle $\alpha = 30^\circ$. For the GLM-CGL with $\mathbf{O2}_{\text{exp}}^{\text{es}}$, $\mathbf{O3}_{\text{exp}}^{\text{es}}$ and $\mathbf{O4}_{\text{exp}}^{\text{es}}$ schemes, the L_1 -errors of B_y are shown in Table(3). We note that every scheme has the desired order of accuracy.

6.6. Orszag-Tang Problem

Following the Orszag-Tang problem for MHD [81, 80, 61], we present a generalized version of the problem for the GLM-CGL (see [41]). The domain for the problem is $[0, 1] \times [0, 1]$, with periodic boundary conditions. The initial state is given as,

$$\begin{aligned}
 (\rho, p_{\parallel}, p_{\perp}, \Psi) &= \left(\frac{25}{36\pi}, \frac{5}{12\pi}, \frac{5}{12\pi}, 0 \right), \\
 \mathbf{v} &= (-\sin(2\pi y), \sin(2\pi x), 0), \\
 \mathbf{B} &= \frac{1}{\sqrt{4\pi}} (-\sin(2\pi y), \sin(4\pi x), 0).
 \end{aligned}$$

It was observed in [41, 40] that the CGL model without the source term (anisotropic case) has difficulty in simulating this test case. Hence, we consider the isotropic CGL and isotropic GLM-CGL cases only. This also makes the solution suitable to compare with the MHD solution.

The numerical results are presented in Figures (3), (4) and (5). We have used 400×400 cells and simulated till the final time $t = 0.5$, using the numerical schemes $\mathbf{O2}_{\text{imex}}^{\text{es}}$, $\mathbf{O3}_{\text{imex}}^{\text{es}}$ and $\mathbf{O4}_{\text{imex}}^{\text{es}}$. From the 2D density plots, we do not see any significant difference between the solutions. However, to observe more closely, we have plotted a one-dimensional cut plot at $y = 0.3125$ of density and p_{\perp} for different schemes and compared with the MHD solutions. All the solutions are similar to the MHD solutions. We observe that all schemes produce solutions that are close to the MHD solution. We further observe that GLM-CGL solutions are slightly more diffusive when compared with CGL solutions of the same order. The numerical results are presented in Figures (3), (4) and (5). We have used 400×400 cells and simulated till the final time $t = 0.5$, using the numerical schemes $\mathbf{O2}_{\text{imex}}^{\text{es}}$, $\mathbf{O3}_{\text{imex}}^{\text{es}}$ and $\mathbf{O4}_{\text{imex}}^{\text{es}}$. From the 2D density plots, we do not see any significant difference between the solutions. However, to observe more closely, we have plotted a one-dimensional cut plot at $y = 0.3125$ of density and p_{\perp} for different schemes and compared with the MHD solutions. All the isotropic solutions are close to the MHD solution. We further observe that GLM-CGL solutions are slightly more diffusive when compared with CGL solutions of the same order.

In Figure (3), we observed that the divergence errors for the GLM-CGL model are significantly lower than the CGL model (almost one-third) for all the schemes. This is further observed in the Figure (4), where we have plotted the time evolution of the L_1 and L_2 errors for divergence of the magnetic field. We again observe that the GLM-CGL divergence errors are significantly lower than the CGL case, for all orders.

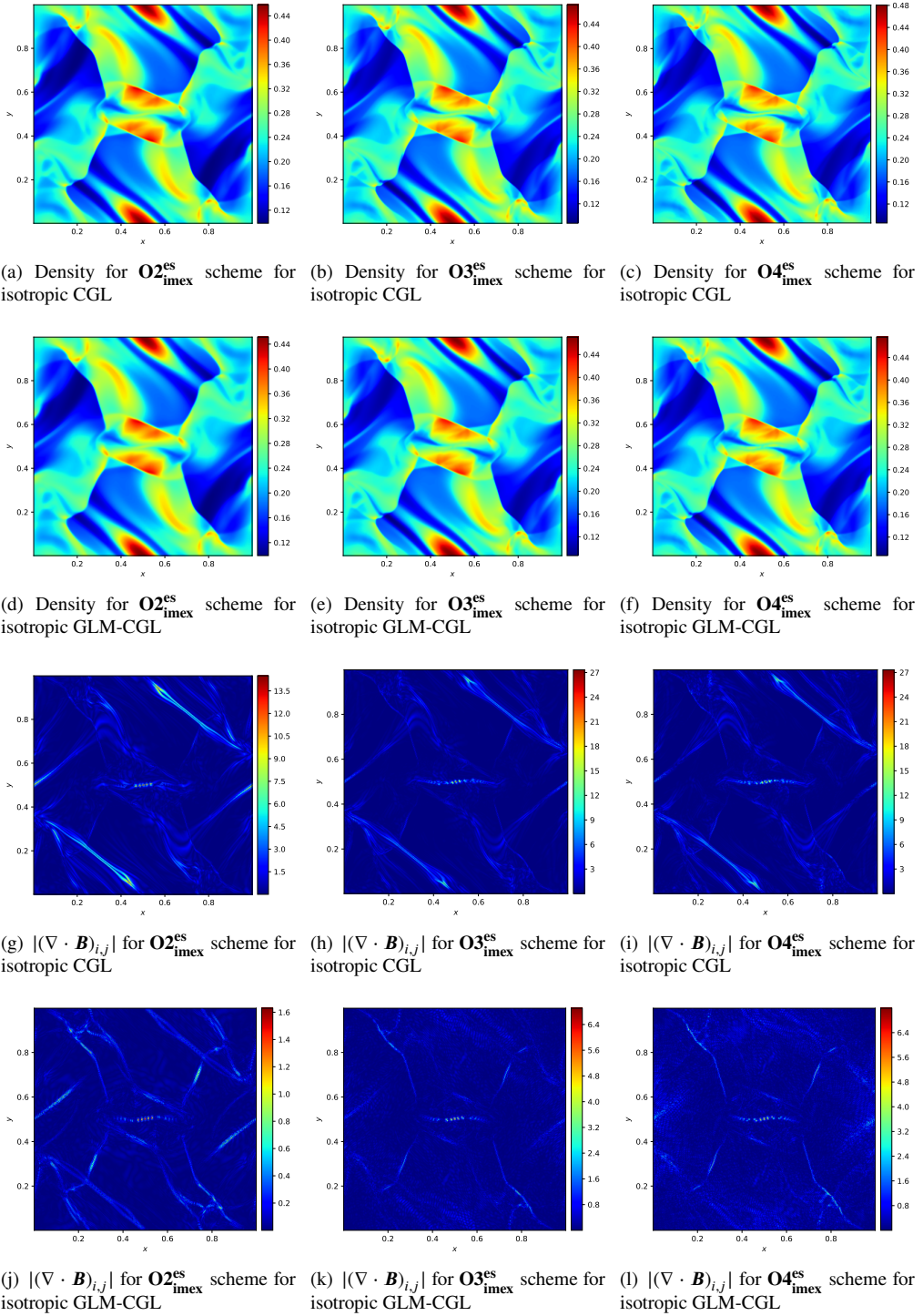
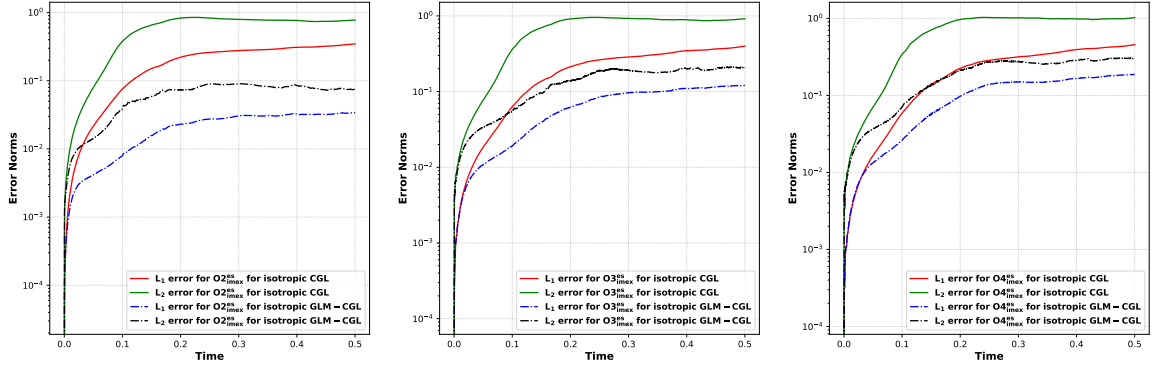
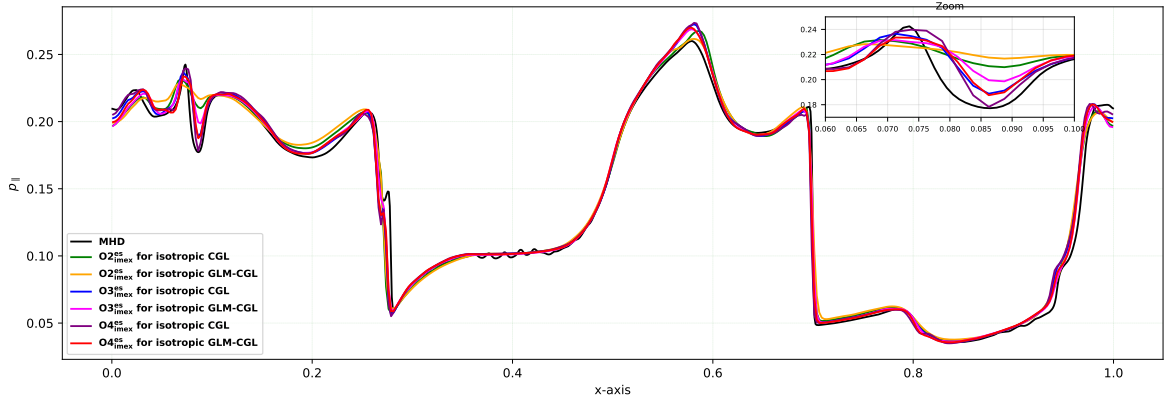


Figure 3: Orszag-Tang Problem: Plots of density and $|\nabla \cdot \mathbf{B}|_{i,j}$ for $\mathbf{O2}_{\text{imex}}^{\text{es}}$, $\mathbf{O3}_{\text{imex}}^{\text{es}}$ and $\mathbf{O4}_{\text{imex}}^{\text{es}}$ schemes for isotropic CGL and isotropic GLM-CGL at time $t = 0.5$.

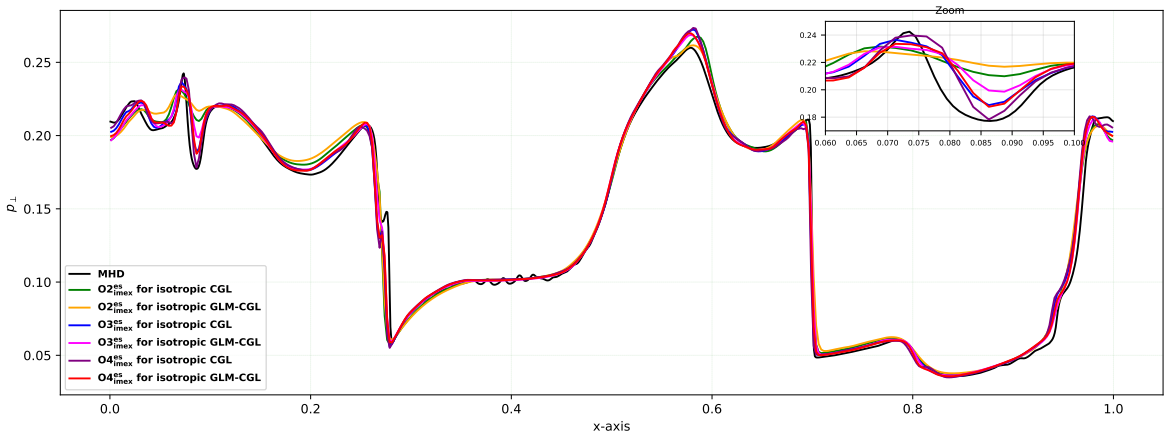


(a) $\|\nabla \cdot \mathbf{B}\|_1$ and $\|\nabla \cdot \mathbf{B}\|_2$ for $O2_{\text{imex}}^{\text{es}}$ scheme for isotropic CGL and isotropic GLM-CGL (b) $\|\nabla \cdot \mathbf{B}\|_1$ and $\|\nabla \cdot \mathbf{B}\|_2$ for $O3_{\text{imex}}^{\text{es}}$ scheme for isotropic CGL and isotropic GLM-CGL (c) $\|\nabla \cdot \mathbf{B}\|_1$ and $\|\nabla \cdot \mathbf{B}\|_2$ for $O4_{\text{imex}}^{\text{es}}$ scheme for isotropic CGL and isotropic GLM-CGL

Figure 4: Orszag-Tang Problem: Evolution of the magnetic field divergence constraint errors till time $t = 0.5$.



(a) Cut of pressure component p_{\parallel} for isotropic CGL and isotropic GLM-CGL along $y = 0.3125$



(b) Cut of pressure component p_{\perp} for isotropic CGL and isotropic GLM-CGL along $y = 0.3125$

Figure 5: Orszag-Tang Problem: Cut plots of pressure components along $y = 0.3125$ at time $t = 0.5$.

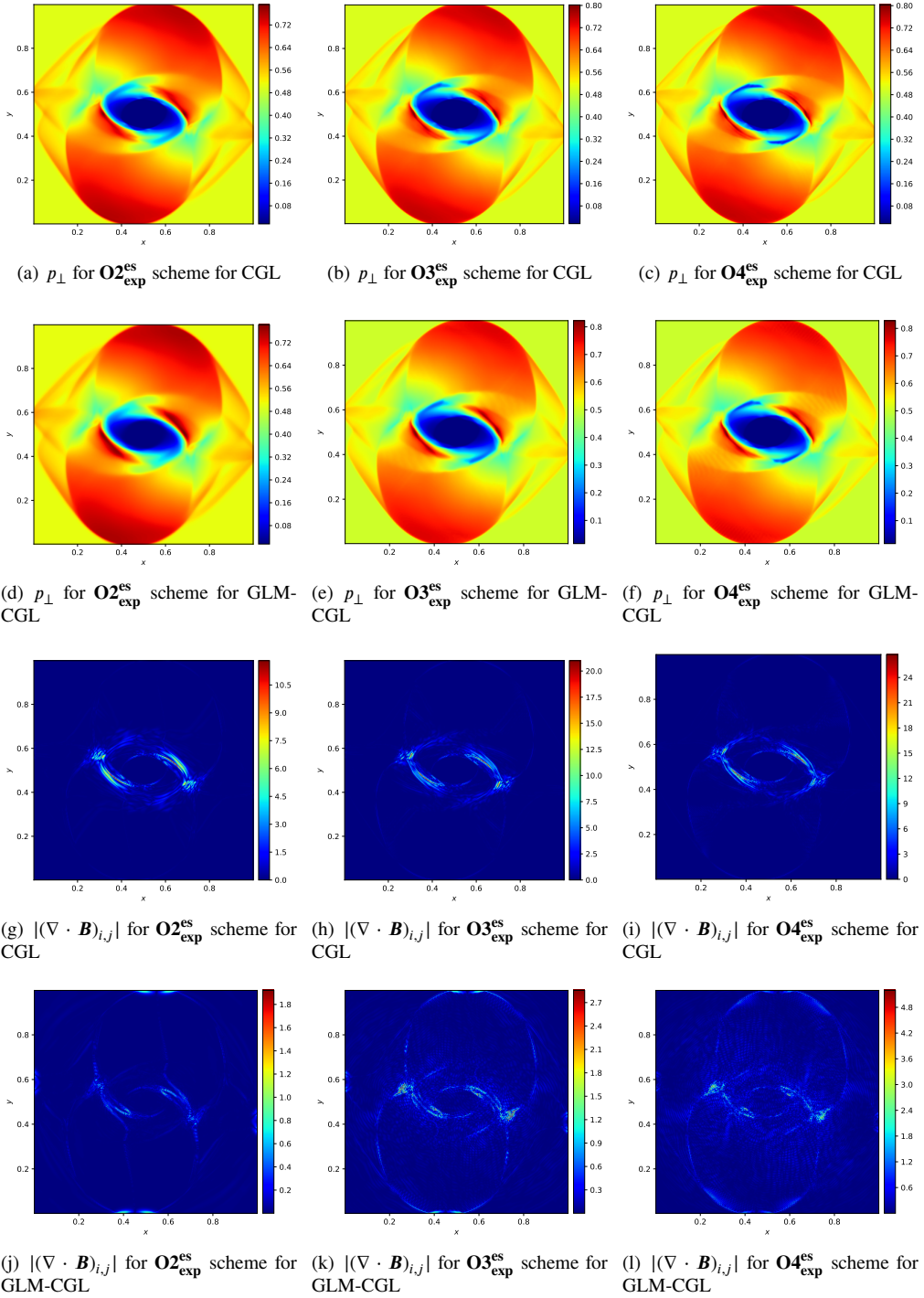


Figure 6: Rotor problem: Plots of p_{\perp} and $|\nabla \cdot \mathbf{B}|_{i,j}$ for $O2_{exp}^{es}$, $O3_{exp}^{es}$ and $O4_{exp}^{es}$ schemes for CGL and GLM-CGL at time $t = 0.295$.

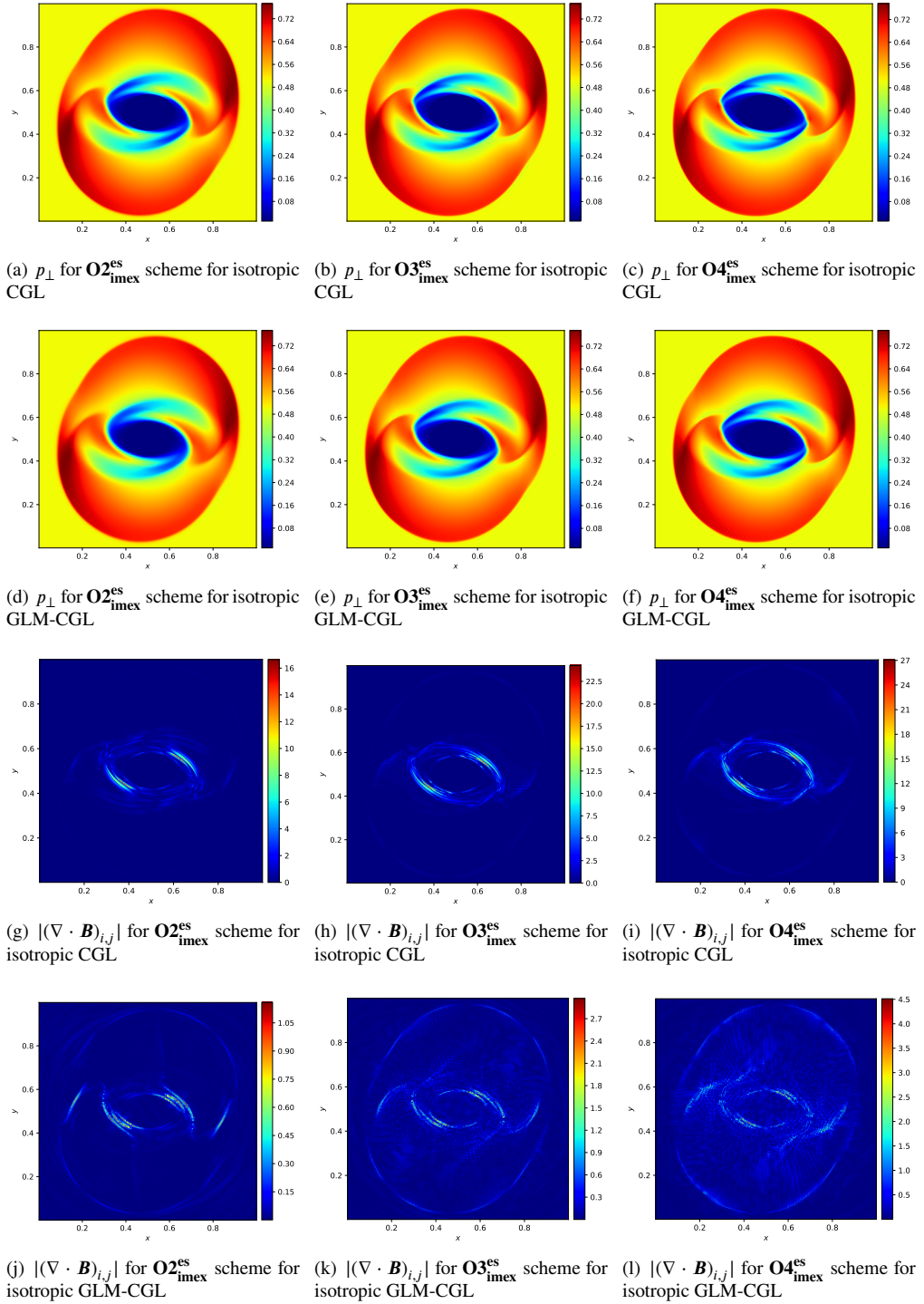
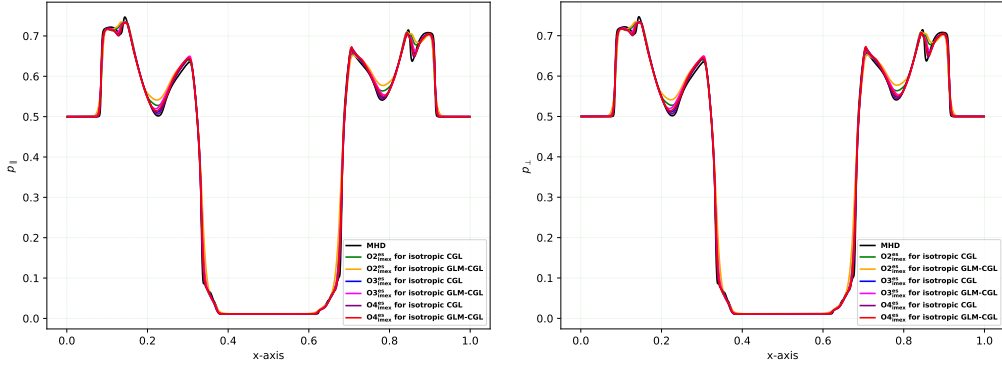
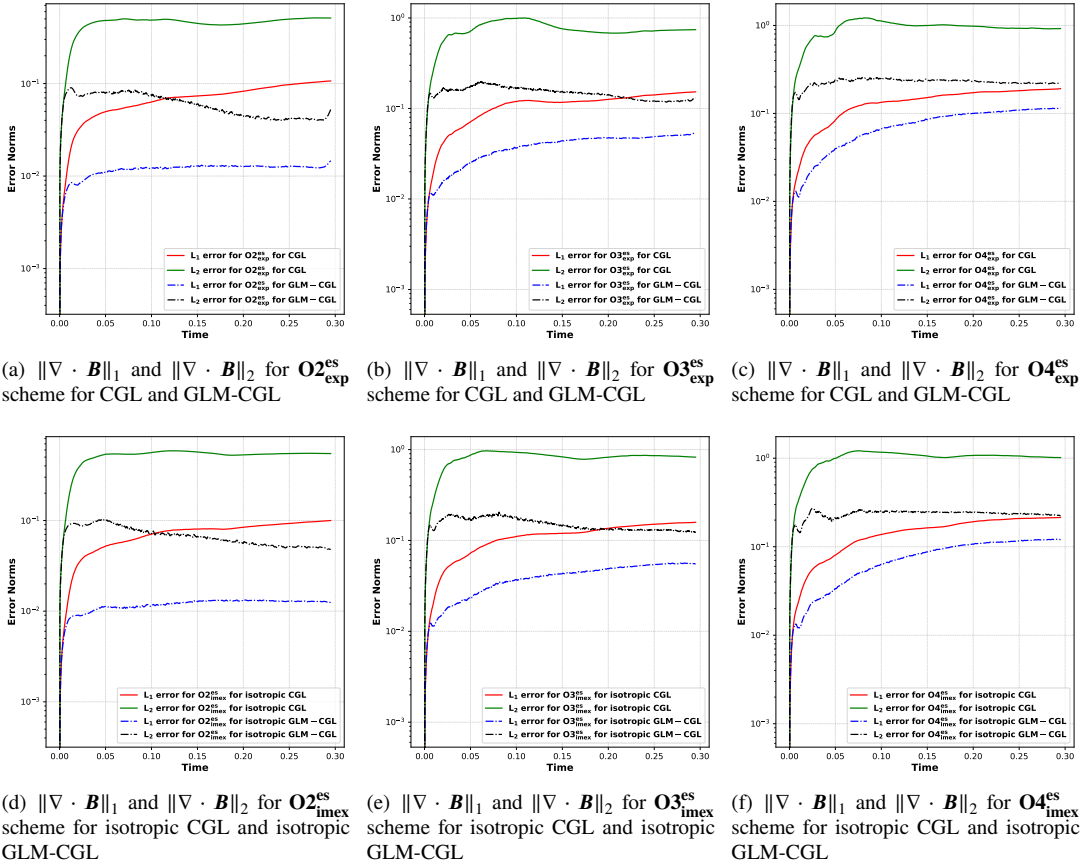


Figure 7: Rotor problem: Plots of p_{\perp} and $|\nabla \cdot \mathbf{B}|_{i,j}$ for $\mathbf{O2}_{\text{imex}}^{\text{es}}$, $\mathbf{O3}_{\text{imex}}^{\text{es}}$ and $\mathbf{O4}_{\text{imex}}^{\text{es}}$ schemes for isotropic CGL and isotropic GLM-CGL at time $t = 0.295$.



(a) Cut of pressure component p_{\parallel} for isotropic CGL and isotropic GLM-CGL along $y = 0.489$ using 400×400 cells (b) Cut of pressure component p_{\perp} for isotropic CGL and isotropic GLM-CGL along $y = 0.489$ using 400×400 cells

Figure 8: Rotor problem: Cut plot of pressure components p_{\parallel} and p_{\perp} at time $t = 0.295$.



(a) $\|\nabla \cdot \mathbf{B}\|_1$ and $\|\nabla \cdot \mathbf{B}\|_2$ for $\mathbf{O2}_{\text{exp}}^{\text{es}}$ scheme for CGL and GLM-CGL

(b) $\|\nabla \cdot \mathbf{B}\|_1$ and $\|\nabla \cdot \mathbf{B}\|_2$ for $\mathbf{O3}_{\text{exp}}^{\text{es}}$ scheme for CGL and GLM-CGL

(c) $\|\nabla \cdot \mathbf{B}\|_1$ and $\|\nabla \cdot \mathbf{B}\|_2$ for $\mathbf{O4}_{\text{exp}}^{\text{es}}$ scheme for CGL and GLM-CGL

(d) $\|\nabla \cdot \mathbf{B}\|_1$ and $\|\nabla \cdot \mathbf{B}\|_2$ for $\mathbf{O2}_{\text{imex}}^{\text{es}}$ scheme for isotropic CGL and isotropic GLM-CGL

(e) $\|\nabla \cdot \mathbf{B}\|_1$ and $\|\nabla \cdot \mathbf{B}\|_2$ for $\mathbf{O3}_{\text{imex}}^{\text{es}}$ scheme for isotropic CGL and isotropic GLM-CGL

(f) $\|\nabla \cdot \mathbf{B}\|_1$ and $\|\nabla \cdot \mathbf{B}\|_2$ for $\mathbf{O4}_{\text{imex}}^{\text{es}}$ scheme for isotropic CGL and isotropic GLM-CGL

Figure 9: Rotor problem: Evolution of the magnetic field divergence constraint errors till time $t = 0.295$.

6.7. Rotor problem

Another interesting test case for MHD equations is the rotor test case, which is considered in [48, 54, 80, 57, 82]. Here, we generalize this test to the CGL model. We consider a computational domain of $[0, 1] \times [0, 1]$ with Neumann boundary conditions. The initial density profile is given by,

$$\rho = \begin{cases} 10.0, & \text{if } r < 0.1, \\ 1 + 9f(r), & \text{if } 0.1 \leq r < 0.115, \\ 1.0, & \text{otherwise,} \end{cases}$$

where, $r(x, y) = |(x, y) - (0.5, 0.5)|$ and $f(r) = \frac{23-200r}{3}$. The initial velocity vector is taken to be,

$$\mathbf{v} = \begin{cases} (-10y - 5), (10x - 5), 0, & \text{if } r < 0.1, \\ (-10y - 5)f(r), (10x - 5)f(r), 0, & \text{if } 0.1 \leq r < 0.115, \\ (0, 0, 0), & \text{otherwise.} \end{cases}$$

The rest of the states are taken to be,

$$(p_{\parallel}, p_{\perp}, B_x, B_y, B_z, \Psi) = \left(0.5, 0.5, \frac{2.5}{\sqrt{4\pi}}, 0, 0, 0 \right).$$

The numerical simulations are performed using 400×400 cells till the final time $t = 0.295$. The results for the CGL and GLM-CGL systems are plotted in Figure (6), using $\mathbf{O2}_{\text{exp}}^{\text{es}}$, $\mathbf{O3}_{\text{exp}}^{\text{es}}$ and $\mathbf{O4}_{\text{exp}}^{\text{es}}$ schemes. We see that all the schemes have resolved complicated shock structures in p_{\perp} variable. We have also plotted the absolute value of the magnetic field divergence. When comparing the results of CGL and GLM-CGL, we observe that the GLM-CGL model produces significantly lower divergence error when compared with the CGL model.

In Figure (7), we have plotted the results for the isotropic case using $\mathbf{O2}_{\text{imex}}^{\text{es}}$, $\mathbf{O3}_{\text{imex}}^{\text{es}}$ and $\mathbf{O4}_{\text{imex}}^{\text{es}}$ schemes at 400×400 cells at final time $t = 0.295$. We again see that the solutions are very similar to the MHD case, and all the schemes are able to resolve wave structures. Furthermore, similar to the anisotropic case, the GLM-CGL model produces significantly lower divergence errors. To compare the isotropic solutions with the MHD solution, in Figure (8), we have plotted a one-dimensional cut of the isotropic solutions and compared it with the MHD solution. We observe that both pressure components match the MHD pressure. Again, we also observe that the GLM-CGL solutions are slightly more diffusive than the CGL solutions for the same scheme.

To monitor the divergence error over time, we have plotted the evolution of the L_1 and L_2 errors of the divergence of the magnetic field. We note that the errors are stable; however, GLM-CGL errors are significantly less than the CGL errors for both isotropic and anisotropic cases.

6.8. Field loop advection problem

Following [83, 32], we consider the field loop advection problem for the CGL model. The computation domain for the test case is $[-1, 1] \times [-0.5, 0.5]$ with periodic boundary conditions. The solutions are computed till the final time $t = 2.0$. The initial conditions are given by,

$$(\rho, \mathbf{v}, p_{\parallel}, p_{\perp}, \Psi) = (2 \times 10^6, 1, 2, 0, 2 \times 10^6, 2 \times 10^6, 0)$$

The magnetic field loop is given in the form of a vector potential as

$$A_z(x, y) = \begin{cases} (R - r), & \text{if } r \leq R, \\ 0, & \text{otherwise.} \end{cases}$$

where $r = \sqrt{x^2 + y^2}$ is the distance from the origin and $R = 0.3$. The numerical results are presented in Figures (10), (11) and (12) using 400×200 cells. We have plotted $|\mathbf{B}|^2$ for CGL, GLM-CGL, isotropic CGL and isotropic GLM-CGL. We observe that the third and fourth order schemes are much less diffusive than the second order schemes. From the $|(\nabla \cdot \mathbf{B})_{i,j}|$ plots, we observed that the GLM-CGL model produces much lower values than the CGL model. The time evolution of the L_1 and L_2 divergence of the magnetic field shows that CGL and GLM-CGL models have similar evolutions.

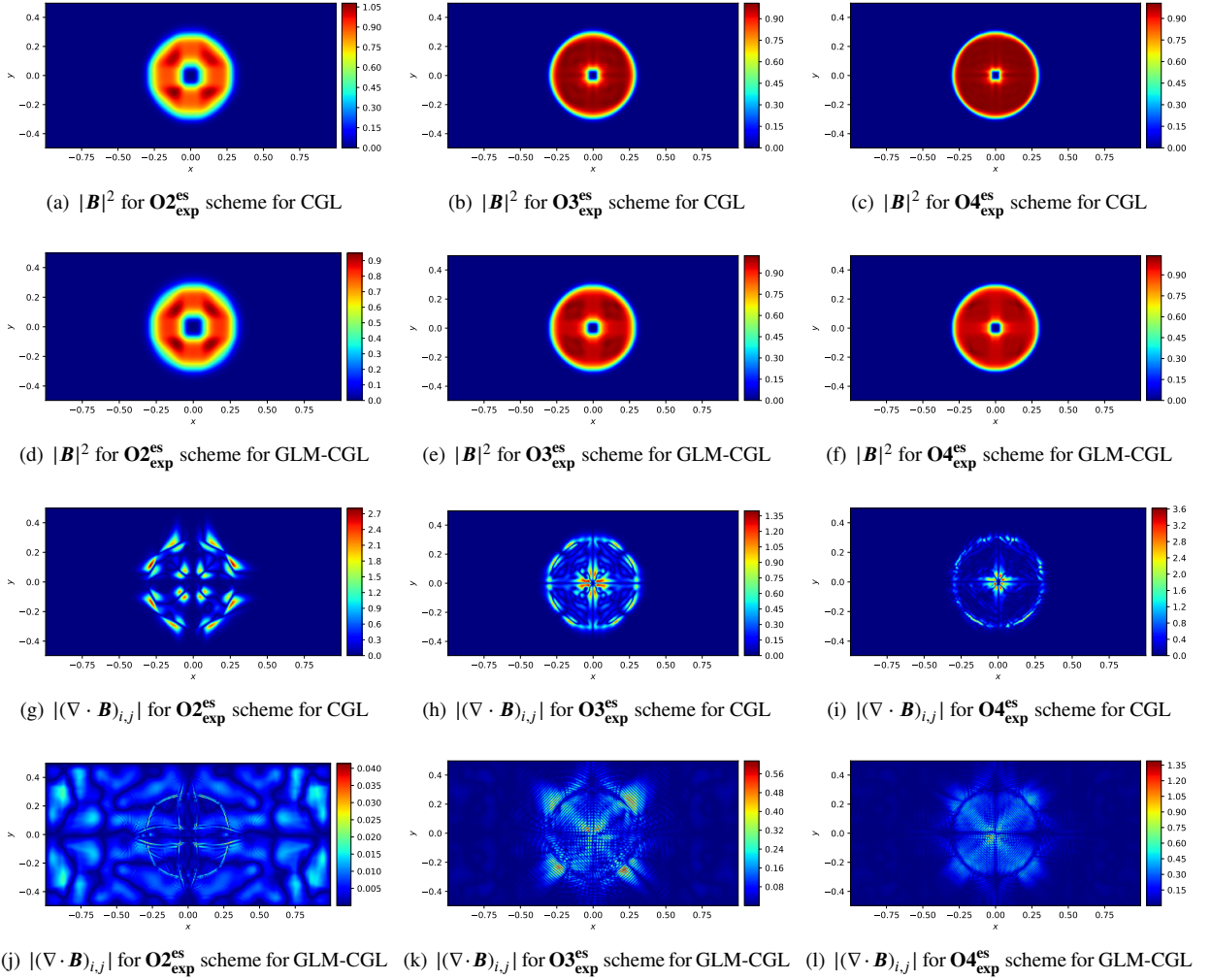


Figure 10: Field loop advection problem: Plots of $|B|^2$ and $|(\nabla \cdot \mathbf{B})_{i,j}|$ for $O2_{\text{exp}}^{\text{es}}$, $O3_{\text{exp}}^{\text{es}}$ and $O4_{\text{exp}}^{\text{es}}$ schemes for CGL and GLM-CGL at time $t = 2.0$.

6.9. CGL Riemann problem

Following MHD Riemann problem in [84, 85], we present the corresponding CGL test case. The computational domain is taken to be $[-0.4, 0.4] \times [-0.4, 0.4]$ with Neumann boundary conditions. The initial conditions are given below:

$$(\rho, p_{\parallel}, p_{\perp}) = \begin{cases} (10, 15, 15), & \text{if } x < 0, y < 0, \\ (1, 0.5, 0.5), & \text{otherwise.} \end{cases}$$

$$(\mathbf{v}, B_x, B_y, B_z, \Psi) = \left(0, 0, 0, \frac{1}{\sqrt{2}}, \frac{1}{\sqrt{2}}, 0, 0 \right).$$

The numerical solutions for B_y are plotted in Figures (13), (14), and (15). We observe that the higher-order schemes are much more accurate than the second-order schemes. We also note that the results of the isotropic cases are similar to the MHD case in [84]. Furthermore, CGL and GLM-CGL results are different from the isotropic case.

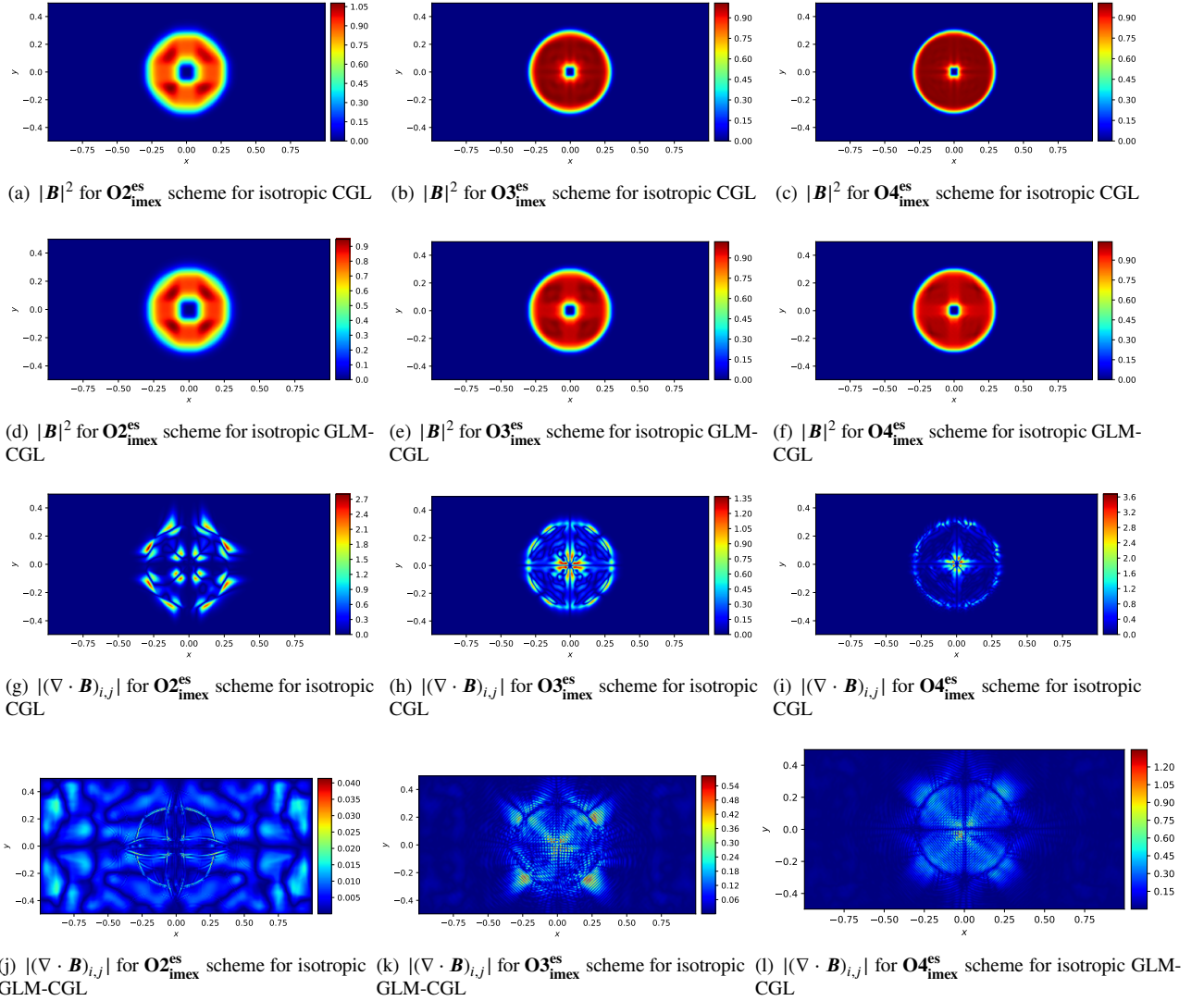


Figure 11: Field loop advection problem: Plots of $|B|^2$ and $|\nabla \cdot \mathbf{B}|_{i,j}$ for $O2_{\text{imex}}^{\text{es}}$, $O3_{\text{imex}}^{\text{es}}$ and $O4_{\text{imex}}^{\text{es}}$ schemes for isotropic CGL and isotropic GLM-CGL at time $t = 2.0$.

From the plots of $|\nabla \cdot \mathbf{B}|_{i,j}$, in Figures (13) and (14), we observe that in each case, GLM-CGL produces much lower values than the CGL case. This is also evident from the time evolution of the L_1 and L_2 norms of the divergence of the magnetic field in Figure (15).

6.10. Two-Dimensional Riemann problem

In the last test case, we consider a two-dimensional Riemann problem with four states, motivated by the similar MHD test case in [86, 85]. We consider a rectangular computational domain given by $[-1.5, 1.5] \times [-1.5, 1.5]$. We

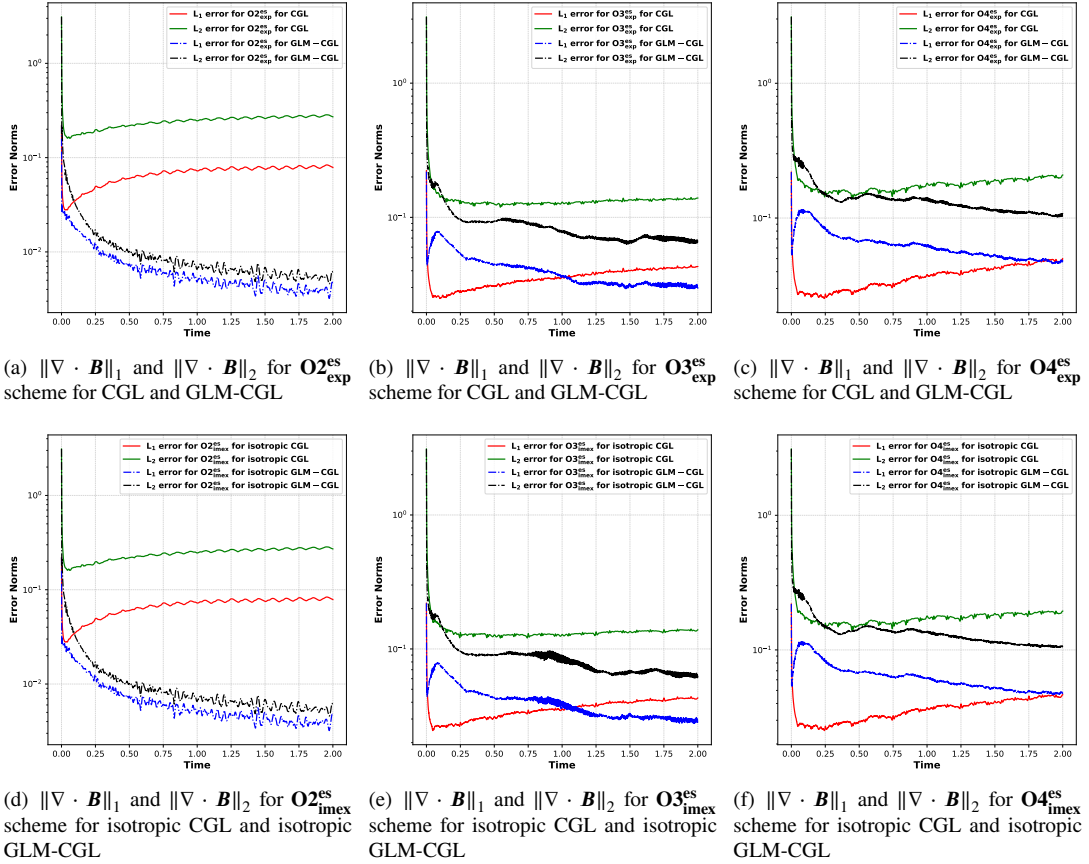


Figure 12: Field loop advection problem: Evolution of the magnetic field divergence constraint errors till time $t = 2.0$.

enforce Neumann boundary conditions. The initial condition consists of four states, which are given as follows:

$$(\rho, \mathbf{v}, p_{\parallel}, p_{\perp}) = \begin{cases} (1, 0.75, -0.5, 0, 1, 1), & \text{if } x > 0, y > 0 \\ (2, 0.75, 0.5, 0, 1, 1), & \text{if } x < 0, y > 0 \\ (1, -0.75, 0.5, 0, 1, 1), & \text{if } x < 0, y < 0 \\ (3, -0.75, -0.5, 0, 1, 1), & \text{if } x > 0, y < 0 \end{cases}$$

$$(B_x, B_y, B_z, \Psi) = \left(\frac{2}{\sqrt{4\pi}}, 0, \frac{1}{\sqrt{4\pi}}, 0 \right).$$

The solutions are computed using 400×400 cells till the final time of $t = 1$. In Fig.(16), we have plotted the schlieren images of B_y and $|(\nabla \cdot \mathbf{B})_{i,j}|$ for CGL and GLM-CGL using $\mathbf{O2}_{\text{exp}}^{\text{es}}$, $\mathbf{O3}_{\text{exp}}^{\text{es}}$ and $\mathbf{O4}_{\text{exp}}^{\text{es}}$ schemes, and in Fig.(17), we have plotted the schlieren image of B_y and $|(\nabla \cdot \mathbf{B})_{i,j}|$ for isotropic CGL and isotropic GLM-CGL using $\mathbf{O2}_{\text{imex}}^{\text{es}}$, $\mathbf{O3}_{\text{imex}}^{\text{es}}$ and $\mathbf{O4}_{\text{imex}}^{\text{es}}$ schemes. We observe that the results for isotropic CGL are similar to those presented in [85]. Furthermore, higher-order schemes produce much sharper solutions than the second-order schemes.

We also compare the $|(\nabla \cdot \mathbf{B})_{i,j}|$ for CGL and GLM-CGL models. In each case, we observe that GLM-CGL produces much lower values of the divergence errors. This can also be observed when we compare the time evolution of the L_1 and L_2 norms divergence of the magnetic fields. We consistently observe that the GLM-CGL produces much lower values than the CGL model in all cases.

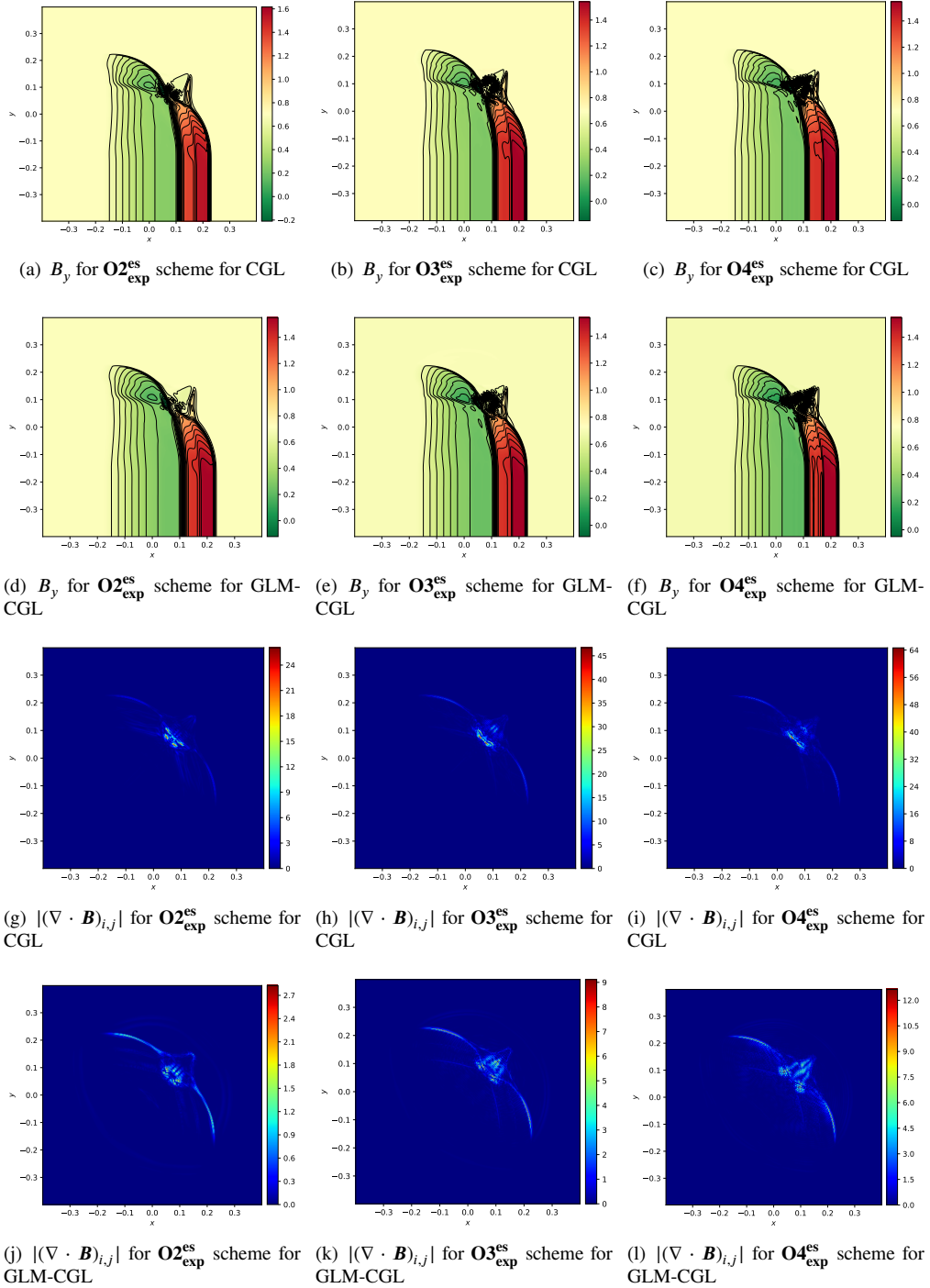


Figure 13: CGL Riemann problem: Plots of B_y and $|(\nabla \cdot \mathbf{B})_{i,j}|$ for $O2_{\text{exp}}^{\text{es}}$, $O3_{\text{exp}}^{\text{es}}$ and $O4_{\text{exp}}^{\text{es}}$ schemes for CGL and GLM-CGL at time $t = 0.1$.

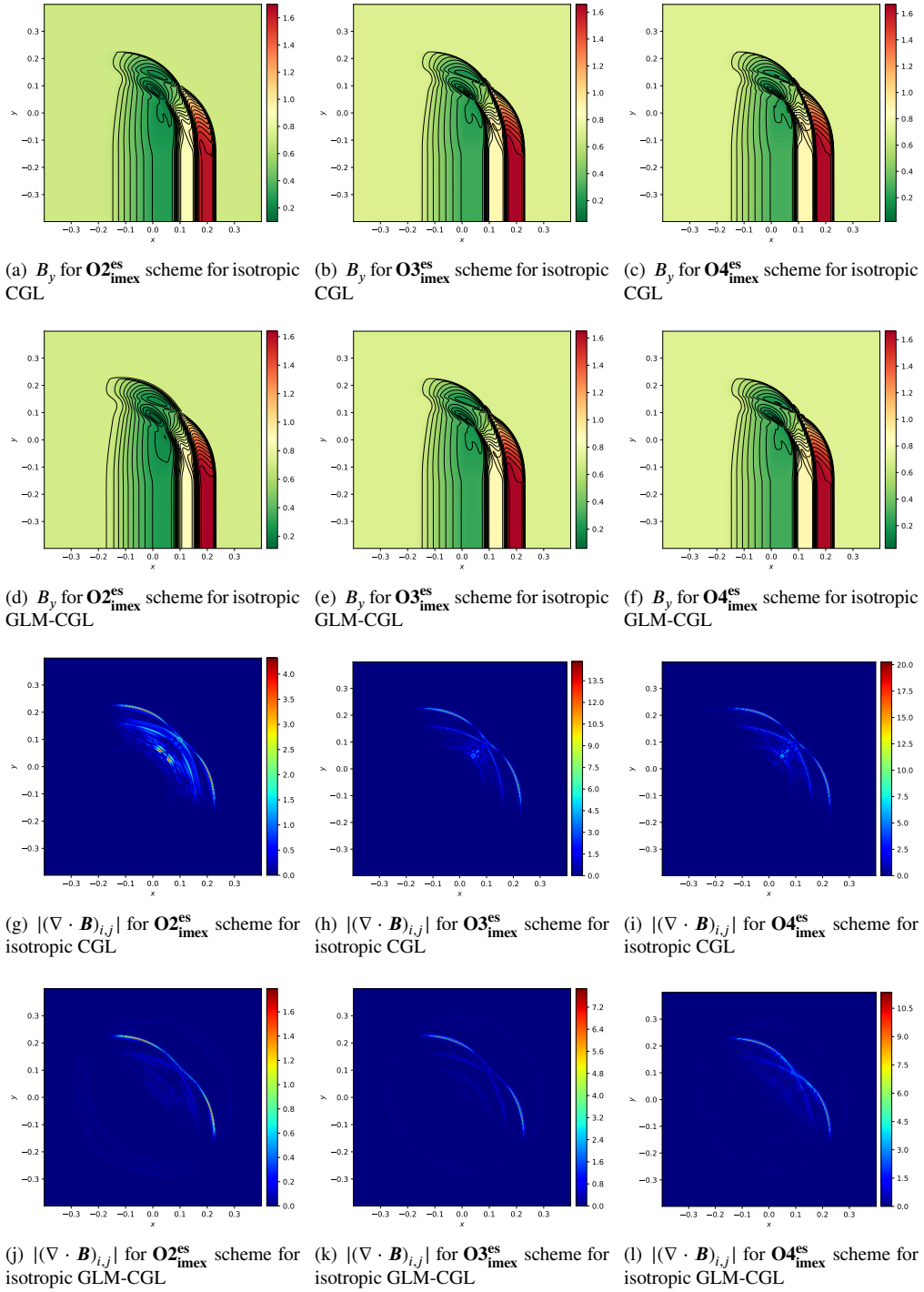


Figure 14: CGL Riemann problem: Plots of B_y and $|\nabla \cdot \mathbf{B}|_{i,j}$ for $O2_{\text{imex}}^{\text{es}}$, $O3_{\text{imex}}^{\text{es}}$ and $O4_{\text{imex}}^{\text{es}}$ schemes for isotropic CGL and isotropic GLM-CGL at time $t = 0.1$.

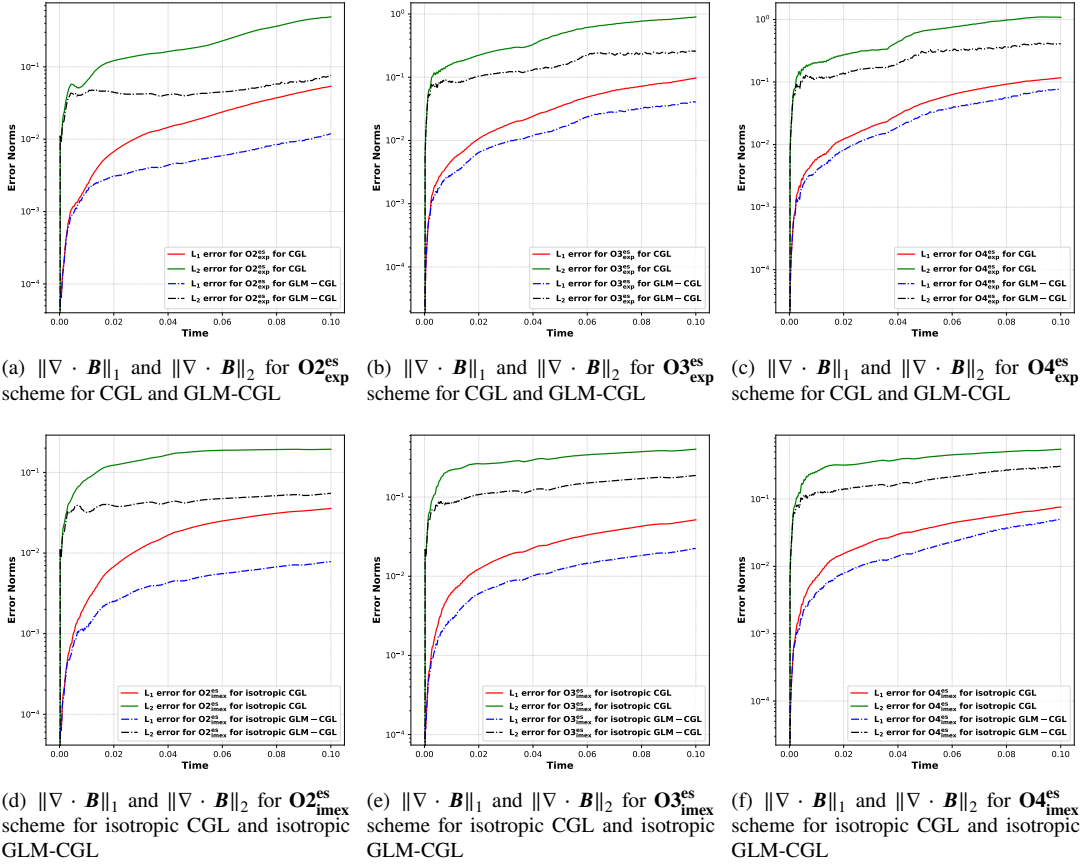


Figure 15: CGL Riemann problem: Evolution of the magnetic field divergence constraint errors till time $t = 0.1$.

7. Conclusion

In this article, we have presented a divergence-diminishing strategy based on the GLM formulation of the CGL equations. This is inspired by a similar strategy for MHD equations. The resulting system is named the GLM-CGL model. We then rewrite the system in such a way that the non-conservative terms do not contribute to entropy production. Furthermore, the conservative part is then symmetrized. The resulting reformulation makes the GLM-CGL system ideal for proposing entropy-stable schemes.

We then design higher-order entropy stable finite difference schemes for the system by designing an entropy conservative flux and a higher-order entropy diffusion operator. The entropy diffusion operator uses the entropy-scaled right eigenvectors. We also consider a source term to compute the isotropic solutions.

For the numerical test cases, we consider several 1D and 2D test cases. We demonstrate that in all the test cases, the proposed schemes have the expected numerical order of accuracy. Also, the isotropic solutions are comparable to the MHD solutions. Furthermore, in each numerical test case, the GLM-CGL formulation is observed to be superior in diminishing the divergence of the magnetic field.

Acknowledgements

Dinshaw S. Balsara and Harish Kumar acknowledge support from a Vajra award (VJR/2018/00129).

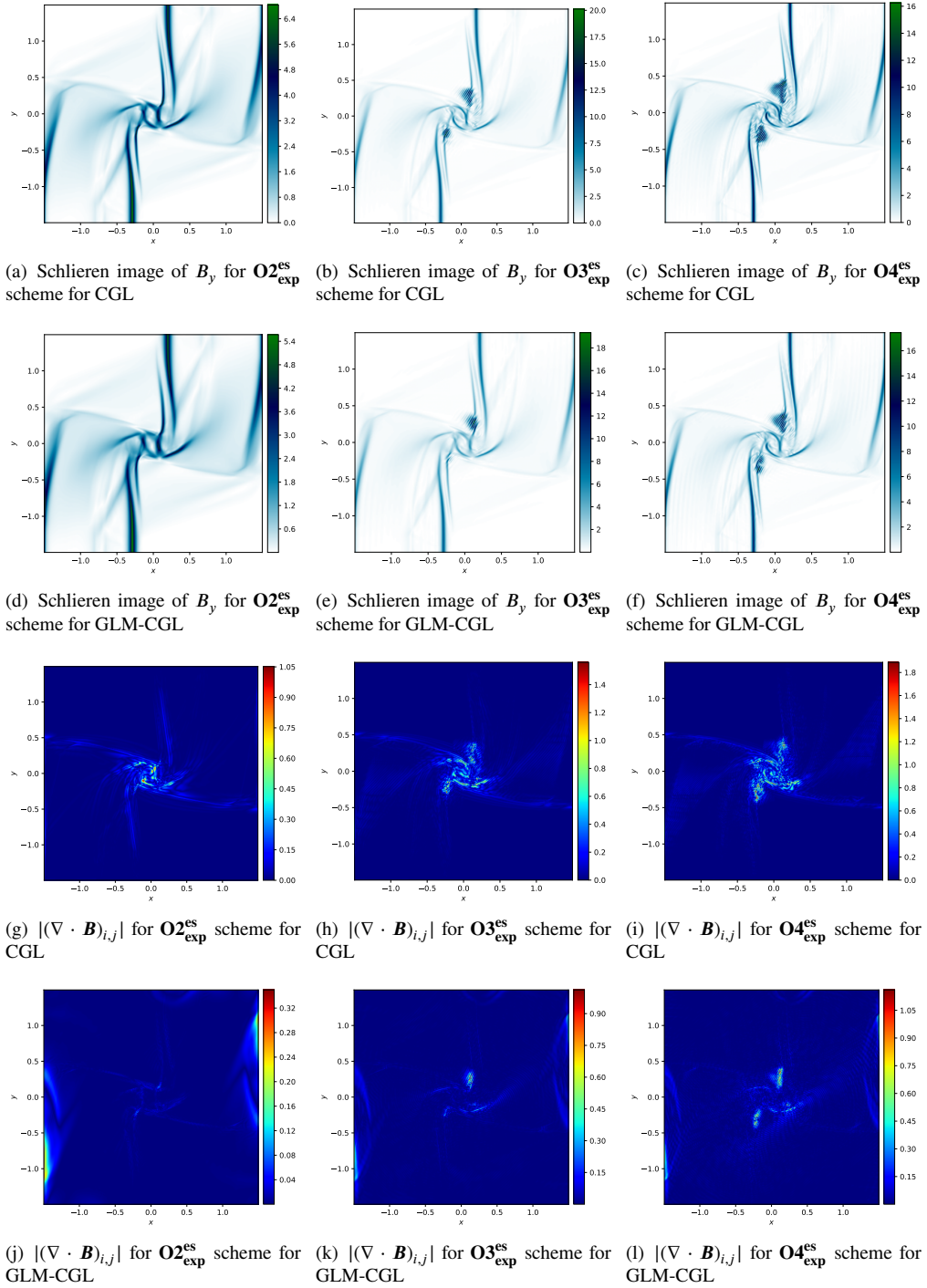


Figure 16: Two-Dimensional Riemann problem: Schlieren image of B_y and plots of $|(\nabla \cdot \mathbf{B})_{i,j}|$ for $O2^{\text{es}}$, $O3^{\text{es}}$ and $O4^{\text{es}}$ schemes for CGL and GLM-CGL at time $t = 1.0$.

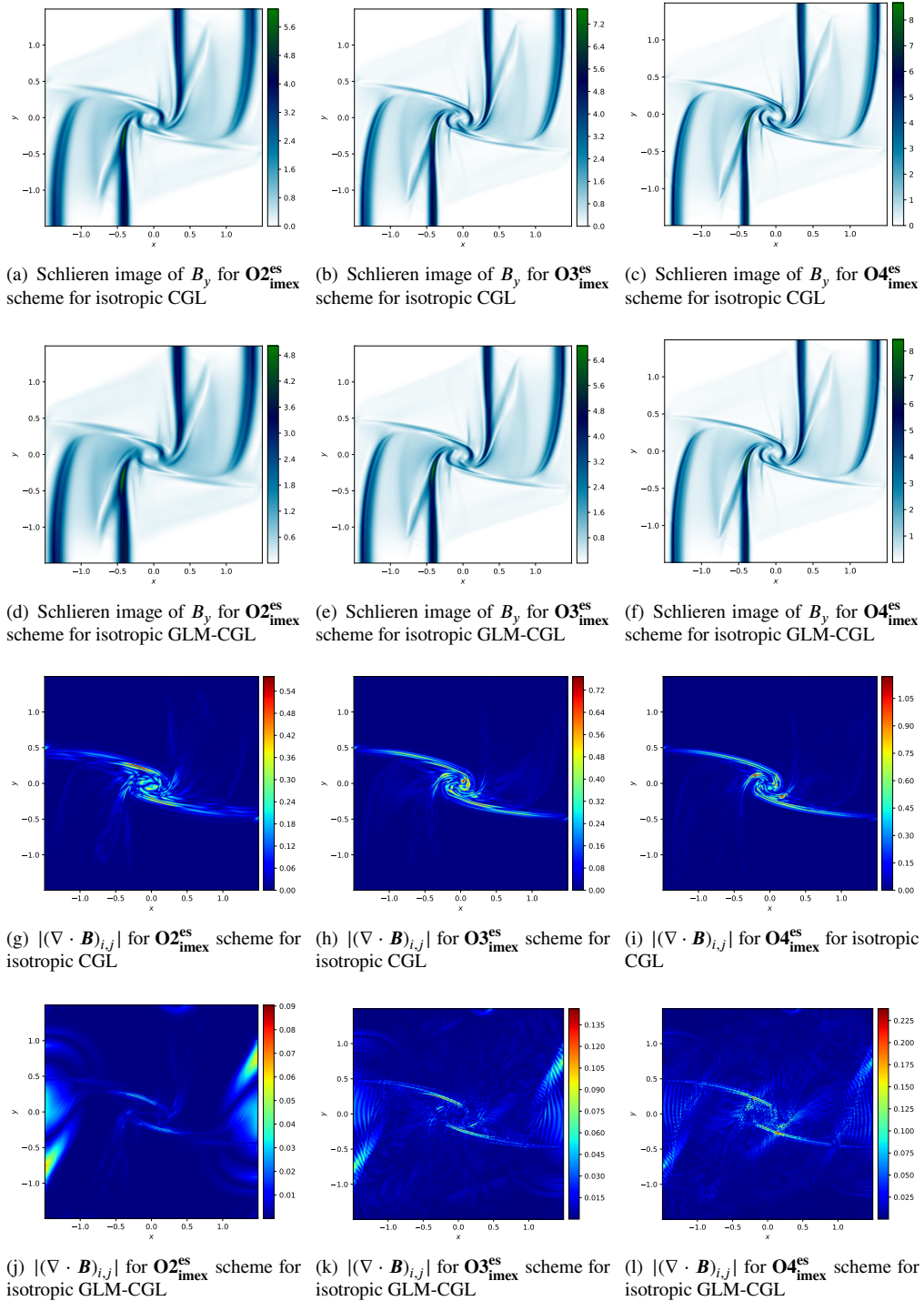


Figure 17: Two-Dimensional Riemann problem: Schlieren image of B_y and plots of $|\nabla \cdot \mathbf{B}|_{i,j}$ for $O2_{imex}^{es}$, $O3_{imex}^{es}$ and $O4_{imex}^{es}$ schemes for isotropic CGL and isotropic GLM-CGL at time $t = 1.0$.

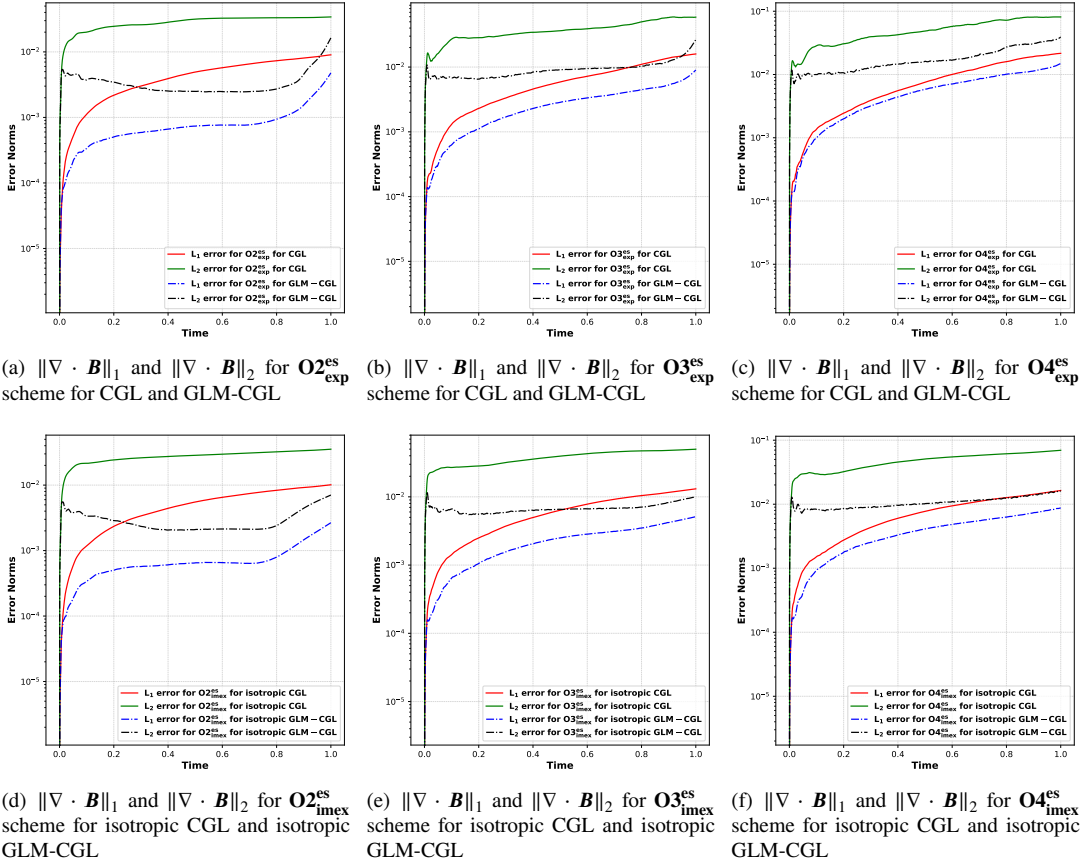


Figure 18: Two-Dimensional Riemann problem: Evolution of the magnetic field divergence constraint errors till time $t = 1.0$.

CRedit authorship contribution statement

Chetan Singh: Formal analysis, Investigation, Methodology, Software, Visualization, Validation, Conceptualization, Writing – original draft. **Harish Kumar:** Conceptualization, Methodology, Supervision, Writing – original draft, Writing – review & editing, Funding acquisition. **Deepak Bhojriya:** Formal analysis, Investigation, Visualization, Software, Writing – review & editing. **Dinshaw S. Balsara:** Conceptualization, Methodology, Supervision, Writing – review & editing, Funding acquisition.

Declarations

Conflict of interest The authors declare that they have no Conflict of interest.

Data availability

Data will be made available on request.

References

- [1] Valery M Nakariakov and Dmitrii Y Kolotkov. Magnetohydrodynamic waves in the solar corona. *Annual Review of Astronomy and Astrophysics*, 58(1):441–481, 2020.
- [2] Claudio Zanni, Attilio Ferrari, Silvano Massaglia, Gianluigi Bodo, and Paola Rossi. On the mhd acceleration of astrophysical jets. *Astrophysics and Space Science*, 293:99–106, 2004.

- [3] Alexander Kosovichev. Astrophysical processes on the sun, 2013.
- [4] Xianzhe Jia, Kenneth C Hansen, Tamas I Gombosi, Margaret G Kivelson, Gabor Tóth, Darren L DeZeeuw, and Aaron J Ridley. Magnetospheric configuration and dynamics of saturn's magnetosphere: A global mhd simulation. *Journal of Geophysical Research: Space Physics*, 117(A5), 2012.
- [5] Xianzhe Jia, Raymond J Walker, Margaret G Kivelson, Krishan K Khurana, and Jon A Linker. Three-dimensional mhd simulations of ganymede's magnetosphere. *Journal of Geophysical Research: Space Physics*, 113(A6), 2008.
- [6] Lev Zelenyi, Helmi Malova, Elena Grigorenko, Victor Popov, and Dominique Delcourt. Current sheets in planetary magnetospheres. *Plasma Physics and Controlled Fusion*, 61(5):054002, 2019.
- [7] Timur J Linde, Tamas I Gombosi, Philip L Roe, Kenneth G Powell, and Darren L DeZeeuw. Heliosphere in the magnetized local interstellar medium: Results of a three-dimensional mhd simulation. *Journal of Geophysical Research: Space Physics*, 103(A2):1889–1904, 1998.
- [8] Laxman Adhikari, Gary P Zank, and Lingling Zhao. The transport and evolution of mhd turbulence throughout the heliosphere: models and observations. *Fluids*, 6(10):368, 2021.
- [9] VV Izmodenov and DB Alexashov. Three-dimensional kinetic-mhd model of the global heliosphere with the heliopause-surface fitting. *The Astrophysical Journal Supplement Series*, 220(2):32, 2015.
- [10] Klaus Scherer, Lennart R Baalmann, Horst Fichtner, Jens Kleimann, Dominik J Bomans, Kerstin Weis, Stefan ES Ferreira, and Konstantin Herbst. Mhd-shock structures of astrospheres: λ cephei-like astrospheres. *Monthly Notices of the Royal Astronomical Society*, 493(3):4172–4185, 2020.
- [11] D MA Meyer, A Mignone, M Petrov, K Scherer, PF Velázquez, and P Boumis. 3d mhd astrospheres: applications to irc-10414 and betelgeuse. *Monthly Notices of the Royal Astronomical Society*, 506(4):5170–5189, 2021.
- [12] Lennart R Baalmann, Klaus Scherer, Jens Kleimann, Horst Fichtner, Dominik J Bomans, and Kerstin Weis. Modelling o-star astrospheres with different relative speeds between the ism and the star: 2d and 3d mhd model comparison. *Astronomy & Astrophysics*, 663:A10, 2022.
- [13] Alexander A Schekochihin. Mhd turbulence: a biased review. *Journal of Plasma Physics*, 88(5):155880501, 2022.
- [14] Joël Sommeria and René Moreau. Why, how, and when, mhd turbulence becomes two-dimensional. *Journal of Fluid Mechanics*, 118:507–518, 1982.
- [15] Dieter Biskamp. *Magnetohydrodynamic turbulence*. Cambridge University Press, 2003.
- [16] Romain Teyssier and Benoît Commerçon. Numerical methods for simulating star formation. *Frontiers in Astronomy and Space Sciences*, 6:51, 2019.
- [17] Eden Girma and Romain Teyssier. A new star formation recipe for magnetohydrodynamics simulations of galaxy formation. *Monthly Notices of the Royal Astronomical Society*, 527(3):6779–6794, 2024.
- [18] Masahiro N Machida, Tomoaki Matsumoto, and Shu-ichiro Inutsuka. Magnetohydrodynamics of population iii star formation. *The Astrophysical Journal*, 685(2):690, 2008.
- [19] Eliot Quataert. Radiatively inefficient accretion flow models of sgr a. *Astronomische Nachrichten: Astronomical Notes*, 324(S1):435–443, 2003.
- [20] SETSUO Ichimaru. Bimodal behavior of accretion disks-theory and application to cygnus x-1 transitions. *The Astrophysical Journal*, 214:840–855, 1977.
- [21] Benjamin DG Chandran, Timothy J Dennis, Eliot Quataert, and Stuart D Bale. Incorporating kinetic physics into a two-fluid solar-wind model with temperature anisotropy and low-frequency alfvén-wave turbulence. *The Astrophysical Journal*, 743(2):197, 2011.
- [22] Joseph V Hollweg. Collisionless electron heat conduction in the solar wind. *Journal of Geophysical Research*, 81(10):1649–1658, 1976.
- [23] Ioannis Zouganelis, Milan Maksimovic, N Meyer-Vernet, Hervé Lamy, and Karine Issautier. A transonic collisionless model of the solar wind. *The Astrophysical Journal*, 606(1):542, 2004.
- [24] JL Burch, TE Moore, RB Torbert, and BL-https Giles. Magnetospheric multiscale overview and science objectives. *Space Science Reviews*, 199:5–21, 2016.
- [25] Homa Karimabadi, V Roytershteyn, HX Vu, YA Omelchenko, J Scudder, W Daughton, Andrew Dimmock, K Nykyri, M Wan, D Sibeck, et al. The link between shocks, turbulence, and magnetic reconnection in collisionless plasmas. *Physics of Plasmas*, 21(6), 2014.
- [26] Yu V Dumin. The corotation field in collisionless magnetospheric plasma and its influence on average electric field in the lower atmosphere. *Advances in Space Research*, 30(10):2209–2214, 2002.
- [27] M Heinemann. Role of collisionless heat flux in magnetospheric convection. *Journal of Geophysical Research: Space Physics*, 104(A12):28397–28410, 1999.
- [28] Chhanda Sen and Harish Kumar. Entropy Stable Schemes For Ten-Moment Gaussian Closure Equations. *Journal of Scientific Computing*, 75(2):1128–1155, May 2018.
- [29] Asha Kumari Meena, Harish Kumar, and Praveen Chandrashekar. Positivity-preserving high-order discontinuous Galerkin schemes for Ten-Moment Gaussian closure equations. *Journal of Computational Physics*, 339:370–395, June 2017.
- [30] Asha Kumari Meena and Harish Kumar. Robust numerical schemes for two-fluid ten-moment plasma flow equations. *Zeitschrift für angewandte Mathematik und Physik*, 70:1–30, 2019.
- [31] Ammar H Hakim. Extended mhd modelling with the ten-moment equations. *Journal of Fusion Energy*, 27:36–43, 2008.
- [32] Kota Hirabayashi, Masahiro Hoshino, and Takanobu Amano. A new framework for magnetohydrodynamic simulations with anisotropic pressure. *Journal of Computational Physics*, 327:851–872, 12 2016.
- [33] Zhenguang Huang, Gábor Tóth, Bart van der Holst, Yuxi Chen, and Tamas Gombosi. A six-moment multi-fluid plasma model. *Journal of Computational Physics*, 387:134–153, 2019.
- [34] GF Chew, ML Goldberger, and FE Low. The boltzmann equation and the one-fluid hydromagnetic equations in the absence of particle collisions. *Proceedings of the Royal Society of London. Series A. Mathematical and Physical Sciences*, 236(1204):112–118, 1956.
- [35] P Hunana, A Tenerani, GP Zank, E Kholmenko, ML Goldstein, GM Webb, PS Cally, M Collados, M Velli, and L Adhikari. An introductory guide to fluid models with anisotropic temperatures. part 1. cgl description and collisionless fluid hierarchy. *Journal of Plasma Physics*,

- 85(6):205850602, 2019.
- [36] GM Webb, SC Anco, SV Meleshko, and GP Zank. Action principles and conservation laws for chew–goldberger–low anisotropic plasmas. *Journal of Plasma Physics*, 88(4):835880402, 2022.
- [37] Xing Meng, Gábor Tóth, Igor V Sokolov, and Tamas I Gombosi. Classical and semirelativistic magnetohydrodynamics with anisotropic ion pressure. *Journal of Computational Physics*, 231(9):3610–3622, 2012.
- [38] Gianni Dal Maso, Philippe G Lefloch, and François Murat. Definition and weak stability of nonconservative products. *Journal de mathématiques pures et appliquées*, 74(6):483–548, 1995.
- [39] Rémi Abgrall and Smadar Karni. A comment on the computation of non-conservative products. *Journal of Computational Physics*, 229(8):2759–2763, 2010.
- [40] Deepak Bhoriya, Dinshaw Balsara, Vladimir Florinski, and Harish Kumar. Going beyond the mhd approximation: Physics-based numerical solution of the cgl equations. *The Astrophysical Journal*, 970(2):154, jul 2024.
- [41] Chetan Singh, Anshu Yadav, Deepak Bhoriya, Harish Kumar, and Dinshaw S Balsara. Entropy stable finite difference schemes for chew, goldberger and low anisotropic plasma flow equations. *Journal of Scientific Computing*, 102(2):51, 2025.
- [42] Vladimir Florinski, Dinshaw S Balsara, Deepak Bhoriya, Gary P Zank, Shishir Biswas, Swati Sharma, and Sethupathy Subramanian. An anisotropic plasma model of the heliospheric interface. *The Astrophysical Journal*, 985(1):6, 2025.
- [43] Chetan Singh, Deepak Bhoriya, Anshu Yadav, Harish Kumar, and Dinshaw S Balsara. Chew, goldberger & low equations: Eigensystem analysis and applications to one-dimensional test problems. *Computers & Mathematics with Applications*, 188:195–220, 2025.
- [44] Dinshaw S Balsara, Deepak Bhoriya, Chi-Wang Shu, and Harish Kumar. Efficient alternative finite difference weno schemes for hyperbolic conservation laws. *Communications on Applied Mathematics and Computation*, pages 1–54, 2024.
- [45] Dinshaw S Balsara, Deepak Bhoriya, Chi-Wang Shu, and Harish Kumar. Efficient alternative finite difference weno schemes for hyperbolic systems with non-conservative products. *Communications on Applied Mathematics and Computation*, pages 1–50, 2024.
- [46] Jeremiah U Brackbill and Daniel C Barnes. The effect of nonzero $\nabla \cdot \mathbf{B}$ on the numerical solution of the magnetohydrodynamic equations. *Journal of Computational Physics*, 35(3):426–430, 1980.
- [47] Jeremiah Brackbill. Fluid modeling of magnetized plasmas. *Space Science Reviews*, 42(1):153–167, 1985.
- [48] Dinshaw S Balsara and Daniel S Spicer. A staggered mesh algorithm using high order godunov fluxes to ensure solenoidal magnetic fields in magnetohydrodynamic simulations. *Journal of Computational Physics*, 149(2):270–292, 1999.
- [49] C-D Munz, Pascal Omnes, Rudolf Schneider, Eric Sonnendrücker, and Ursula Voss. Divergence correction techniques for maxwell solvers based on a hyperbolic model. *Journal of Computational Physics*, 161(2):484–511, 2000.
- [50] Dinshaw S Balsara. Divergence-free adaptive mesh refinement for magnetohydrodynamics. *Journal of Computational Physics*, 174(2):614–648, 2001.
- [51] Andreas Dedner, Friedemann Kemm, Dietmar Kröner, C-D Munz, Thomas Schnitzer, and Matthias Wesenberg. Hyperbolic divergence cleaning for the mhd equations. *Journal of Computational Physics*, 175(2):645–673, 2002.
- [52] Dinshaw S Balsara, Rakesh Kumar, and Praveen Chandrashekar. Globally divergence-free dg scheme for ideal compressible mhd. *Communications in Applied Mathematics and Computational Science*, 16(1):59–98, 2021.
- [53] Fengyan Li and Chi-Wang Shu. Locally divergence-free discontinuous galerkin methods for mhd equations. *Journal of Scientific Computing*, 22:413–442, 2005.
- [54] Dinshaw S Balsara. Second-order-accurate schemes for magnetohydrodynamics with divergence-free reconstruction. *The Astrophysical Journal Supplement Series*, 151(1):149, 2004.
- [55] Dinshaw S Balsara and Michael Dumbser. Divergence-free mhd on unstructured meshes using high order finite volume schemes based on multidimensional riemann solvers. *Journal of Computational Physics*, 299:687–715, 2015.
- [56] Dinshaw S Balsara, Tobias Rumpf, Michael Dumbser, and Claus-Dieter Munz. Efficient, high accuracy ader-weno schemes for hydrodynamics and divergence-free magnetohydrodynamics. *Journal of Computational Physics*, 228(7):2480–2516, 2009.
- [57] Dominik Derigs, Andrew R Winters, Gregor J Gassner, Stefanie Walch, and Marvin Bohm. Ideal glm-mhd: about the entropy consistent nine-wave magnetic field divergence diminishing ideal magnetohydrodynamics equations. *Journal of Computational Physics*, 364:420–467, 2018.
- [58] Andrés M Rueda-Ramírez, Aleksey Sikstel, and Gregor J Gassner. An entropy-stable discontinuous galerkin discretization of the ideal multi-ion magnetohydrodynamics system. *Journal of Computational Physics*, 523:113655, 2025.
- [59] Andrea Mignone, Petros Tzeferacos, and Gianluigi Bodo. High-order conservative finite difference glm–mhd schemes for cell-centered mhd. *Journal of Computational Physics*, 229(17):5896–5920, 2010.
- [60] Dinshaw S Balsara, Deepak Bhoriya, Chetan Singh, Harish Kumar, Roger Käppeli, and Federico Gatti. Physical constraint preserving higher order finite volume schemes for divergence-free astrophysical mhd and rmhd. *The Astrophysical Journal*, 988:134, 2025.
- [61] Praveen Chandrashekar and Christian Klingenberg. Entropy stable finite volume scheme for ideal compressible mhd on 2-d cartesian meshes. *SIAM Journal on Numerical Analysis*, 54(2):1313–1340, 2016.
- [62] Ulrik S Fjordholm, Siddhartha Mishra, and Eitan Tadmor. Eno reconstruction and eno interpolation are stable. *Foundations of Computational Mathematics*, 13(2):139–159, 2013.
- [63] Margarete O Domingues, Anna Karina F Gomes, SM Gomes, O Mendes, B Di Pierro, and K Schneider. Extended generalized lagrangian multipliers for magnetohydrodynamics using adaptive multiresolution methods. In *ESAIM: Proceedings*, volume 43, pages 95–107. EDP Sciences, 2013.
- [64] Jonathan Mackey and Andrew J Lim. Effects of magnetic fields on photoionized pillars and globules. *Monthly Notices of the Royal Astronomical Society*, 412(3):2079–2094, 2011.
- [65] Terrence S Tricco and Daniel J Price. Constrained hyperbolic divergence cleaning for smoothed particle magnetohydrodynamics. *Journal of Computational Physics*, 231(21):7214–7236, 2012.

- [66] Terrence S Tricco, Daniel J Price, and Matthew R Bate. Constrained hyperbolic divergence cleaning in smoothed particle magnetohydrodynamics with variable cleaning speeds. *Journal of Computational Physics*, 322:326–344, 2016.
- [67] Anshu Yadav, Deepak Bhoriya, Harish Kumar, and Praveen Chandrashekar. Entropy stable schemes for the shear shallow water model equations. *Journal of Scientific Computing*, 97(3):77, 2023.
- [68] Timothy J Barth. Numerical methods for gasdynamic systems on unstructured meshes. *An Introduction to Recent Developments in Theory and Numerics for Conservation Laws: Proceedings of the International School on Theory and Numerics for Conservation Laws, Freiburg/Littenweiler, October 20–24, 1997*, pages 195–285, 1999.
- [69] Timothy Barth. On the role of involutions in the discontinuous galerkin discretization of maxwell and magnetohydrodynamic systems. *IMA Volumes in Mathematics and its Applications*, 142:69, 2006.
- [70] Dominik Derigs, Andrew R Winters, Gregor J Gassner, and Stefanie Walch. A novel high-order, entropy stable, 3d amr mhd solver with guaranteed positive pressure. *Journal of Computational Physics*, 317:223–256, 2016.
- [71] Sergei K Godunov. Symmetric form of the equations of magnetohydrodynamics. *Numerical Methods for Mechanics of Continuum Medium*, 1:26–34, 1972.
- [72] Eitan Tadmor. Entropy stability theory for difference approximations of nonlinear conservation laws and related time-dependent problems. *Acta Numerica*, 12:451–512, 2003.
- [73] Philippe G Lefloch, Jean-Marc Mercier, and Christian Rohde. Fully discrete, entropy conservative schemes of arbitrary order. *SIAM Journal on Numerical Analysis*, 40(5):1968–1992, 2002.
- [74] Ulrik S Fjordholm, Siddhartha Mishra, and Eitan Tadmor. Arbitrarily high-order accurate entropy stable essentially nonoscillatory schemes for systems of conservation laws. *SIAM Journal on Numerical Analysis*, 50(2):544–573, 2012.
- [75] Sigal Gottlieb, Chi-Wang Shu, and Eitan Tadmor. Strong stability-preserving high-order time discretization methods. *SIAM review*, 43(1):89–112, 2001.
- [76] Lorenzo Pareschi and Giovanni Russo. Implicit–explicit runge–kutta schemes and applications to hyperbolic systems with relaxation. *Journal of Scientific computing*, 25:129–155, 2005.
- [77] Christopher A Kennedy and Mark H Carpenter. Additive runge–kutta schemes for convection–diffusion–reaction equations. *Applied numerical mathematics*, 44(1-2):139–181, 2003.
- [78] Yong Liu, Jianfang Lu, and Chi-Wang Shu. An entropy stable essentially oscillation-free discontinuous galerkin method for solving ideal magnetohydrodynamic equations. *Journal of Computational Physics*, 530:113911, 2025.
- [79] M Brio and C.C Wu. An upwind differencing scheme for the equations of ideal magnetohydrodynamics. *Journal of Computational Physics*, 75(2):400–422, 4 1988.
- [80] Gábor Tóth. The div $\mathbf{b} = 0$ constraint in shock-capturing magnetohydrodynamics codes. *Journal of Computational Physics*, 161(2):605–652, 2000.
- [81] Steven A Orszag and Cha-Mei Tang. Small-scale structure of two-dimensional magnetohydrodynamic turbulence. *Journal of Fluid Mechanics*, 90(1):129–143, 1979.
- [82] Franz Georg Fuchs, Andrew D McMurtry, Siddhartha Mishra, Nils Henrik Risebro, and Knut Waagan. Approximate riemann solvers and robust high-order finite volume schemes for multi-dimensional ideal mhd equations. *Communications in Computational Physics*, 9(2):324–362, 2011.
- [83] Thomas A Gardiner and James M Stone. An unsplit godunov method for ideal mhd via constrained transport. *Journal of Computational Physics*, 205(2):509–539, 2005.
- [84] Manuel Torrilhon. Locally divergence-preserving upwind finite volume schemes for magnetohydrodynamic equations. *SIAM Journal on Scientific Computing*, 26(4):1166–1191, 2005.
- [85] Robert Artebrant and Manuel Torrilhon. Increasing the accuracy in locally divergence-preserving finite volume schemes for mhd. *Journal of computational physics*, 227(6):3405–3427, 2008.
- [86] Wenlong Dai and Paul R Woodward. A simple finite difference scheme for multidimensional magnetohydrodynamical equations. *Journal of Computational Physics*, 142(2):331–369, 1998.
- [87] Yusuke Kato, Masayoshi Tajiri, and Tosiya Taniuti. Propagation of hydromagnetic waves in collisionless plasma. i. *Journal of the Physical Society of Japan*, 21(4):765–777, 1966.

A. Eigenvalues and admissible domain of GLM-CGL system

Following [87, 41, 43], the set of eigenvalues of GLM-CGL system (7) in x -direction is given below,

$$\tilde{\Lambda}_x = \left\{ v_x, v_x, \frac{1}{2} \left(v_x \pm \sqrt{4c_h^2 + v_x^2} \right), v_x \pm c_a, v_x \pm c_f, v_x \pm c_s \right\} \quad (44)$$

where,

$$c_a = \sqrt{\frac{B_x^2}{\rho} - \frac{(p_{\parallel} - p_{\perp})b_x^2}{\rho}},$$

$$c_f = \frac{1}{\sqrt{2\rho}} \left[|\mathbf{B}|^2 + 2p_{\perp} + b_x^2(2p_{\parallel} - p_{\perp}) + \{ (|\mathbf{B}|^2 + 2p_{\perp} + b_x^2(2p_{\parallel} - p_{\perp}))^2 \} \right]$$

$$\begin{aligned}
 & + 4(p_{\perp}^2 b_x^2(1 - b_x^2) - 3p_{\parallel} p_{\perp} b_x^2(2 - b_x^2) + 3p_{\parallel}^2 b_x^4 - 3B_x^2 p_{\parallel}) \}^{\frac{1}{2}}]^{\frac{1}{2}}, \\
 c_s = & \frac{1}{\sqrt{2\rho}} [|\mathbf{B}|^2 + 2p_{\perp} + b_x^2(2p_{\parallel} - p_{\perp}) - \{(|\mathbf{B}|^2 + 2p_{\perp} + b_x^2(2p_{\parallel} - p_{\perp}))^2 \\
 & + 4(p_{\perp}^2 b_x^2(1 - b_x^2) - 3p_{\parallel} p_{\perp} b_x^2(2 - b_x^2) + 3p_{\parallel}^2 b_x^4 - 3B_x^2 p_{\parallel}) \}^{\frac{1}{2}}]^{\frac{1}{2}}.
 \end{aligned}$$

Here, v_x define the entropy and pressure anisotropy wave and $\frac{1}{2} \left(v_x \pm \sqrt{4c_h^2 + v_x^2} \right)$ define the right and left going GLM waves. Similarly, $v_x \pm c_a$ defines the right- and left-going Alfvén waves. Also, $v_x \pm c_f$ and $v_x \pm c_s$ are the right and left going fast and slow waves. In the GLM-CGL system, we have extra eigenvalues corresponding to the right and left going GLM waves, and all other eigenvalues are equal to the CGL system. In [87], the authors show that the CGL system is not always hyperbolic, and additional constraints need to be imposed to ensure hyperbolicity. We define

$$p_m = \frac{p_{\perp}^2}{6p_{\perp} + 3|\mathbf{B}|^2}, \text{ and } p_M = |\mathbf{B}|^2 + p_{\perp}.$$

Then, the admissible domain for the CGL system is given by,

$$\Omega = \{ \mathbf{U} \in \mathbb{R}^{10} \mid \rho > 0, p_{\parallel} > 0, p_{\perp} > 0, p_m \leq p_{\parallel} \leq p_M \}. \quad (45)$$

The solution domain Ω then must be partitioned because it was observed in [87] that the slow wave is not always slower than the Alfvén wave. So, we impose

1. $p_m \leq p_{\parallel} \leq \frac{p_M}{4}$, if $c_s \leq c_a \leq c_f$,
2. $\frac{p_M}{4} \leq p_{\parallel} \leq \frac{p_M}{4} + \frac{3p_m}{4}$, if $c_s \leq c_a < c_f$,
3. $\frac{p_M}{4} + \frac{3p_m}{4} \leq p_{\parallel} \leq p_M$, if $c_a \leq c_s < c_f$.

With these conditions, the system is hyperbolic. As discussed above, the GLM-CGL system will also be hyperbolic under the same assumptions. Similarly, the eigenvalues in y -direction are,

$$\tilde{\Lambda}_y = \left\{ v_y, v_y, \frac{1}{2} \left(v_y \pm \sqrt{4c_h^2 + v_y^2} \right), v_y \pm c_a, v_y \pm c_f, v_y \pm c_s \right\} \quad (46)$$

where,

$$\begin{aligned}
 c_a = & \sqrt{\frac{B_y^2}{\rho} - \frac{(p_{\parallel} - p_{\perp})b_y^2}{\rho}}, \\
 c_f = & \frac{1}{\sqrt{2\rho}} [|\mathbf{B}|^2 + 2p_{\perp} + b_y^2(2p_{\parallel} - p_{\perp}) + \{(|\mathbf{B}|^2 + 2p_{\perp} + b_y^2(2p_{\parallel} - p_{\perp}))^2 \\
 & + 4(p_{\perp}^2 b_y^2(1 - b_y^2) - 3p_{\parallel} p_{\perp} b_y^2(2 - b_y^2) + 3p_{\parallel}^2 b_y^4 - 3B_y^2 p_{\parallel}) \}^{\frac{1}{2}}]^{\frac{1}{2}}, \\
 c_s = & \frac{1}{\sqrt{2\rho}} [|\mathbf{B}|^2 + 2p_{\perp} + b_y^2(2p_{\parallel} - p_{\perp}) - \{(|\mathbf{B}|^2 + 2p_{\perp} + b_y^2(2p_{\parallel} - p_{\perp}))^2 \\
 & + 4(p_{\perp}^2 b_y^2(1 - b_y^2) - 3p_{\parallel} p_{\perp} b_y^2(2 - b_y^2) + 3p_{\parallel}^2 b_y^4 - 3B_y^2 p_{\parallel}) \}^{\frac{1}{2}}]^{\frac{1}{2}}.
 \end{aligned}$$

Following [57], instead of using the above eigenvalues, we consider eigenvalues of the system (32) for the x -direction, which is given below:

$$\Lambda_x = \{ v_x, v_x, v_x \pm c_h, v_x \pm c_a, v_x \pm c_f, v_x \pm c_s \} \quad (47)$$

where,

$$c_a = \sqrt{\frac{B_x^2}{\rho} - \frac{(p_{\parallel} - p_{\perp})b_x^2}{\rho}},$$

$$\begin{aligned}
 c_f &= \frac{1}{\sqrt{2\rho}} \left[|\mathbf{B}|^2 + 2p_\perp + b_x^2(2p_\parallel - p_\perp) + \{(|\mathbf{B}|^2 + 2p_\perp + b_x^2(2p_\parallel - p_\perp))^2 \right. \\
 &\quad \left. + 4(p_\perp^2 b_x^2(1 - b_x^2) - 3p_\parallel p_\perp b_x^2(2 - b_x^2) + 3p_\parallel^2 b_x^4 - 3B_x^2 p_\parallel)\}^{\frac{1}{2}} \right]^{\frac{1}{2}}, \\
 c_s &= \frac{1}{\sqrt{2\rho}} \left[|\mathbf{B}|^2 + 2p_\perp + b_x^2(2p_\parallel - p_\perp) - \{(|\mathbf{B}|^2 + 2p_\perp + b_x^2(2p_\parallel - p_\perp))^2 \right. \\
 &\quad \left. + 4(p_\perp^2 b_x^2(1 - b_x^2) - 3p_\parallel p_\perp b_x^2(2 - b_x^2) + 3p_\parallel^2 b_x^4 - 3B_x^2 p_\parallel)\}^{\frac{1}{2}} \right]^{\frac{1}{2}}.
 \end{aligned}$$

We consider eigenvalues of the system (32) for y -direction, which is given below:

$$\Lambda_y = \{v_y, v_y, v_y \pm c_h, v_y \pm c_a, v_y \pm c_f, v_y \pm c_s\} \quad (48)$$

where,

$$\begin{aligned}
 c_a &= \sqrt{\frac{B_y^2}{\rho} - \frac{(p_\parallel - p_\perp)b_y^2}{\rho}}, \\
 c_f &= \frac{1}{\sqrt{2\rho}} \left[|\mathbf{B}|^2 + 2p_\perp + b_y^2(2p_\parallel - p_\perp) + \{(|\mathbf{B}|^2 + 2p_\perp + b_y^2(2p_\parallel - p_\perp))^2 \right. \\
 &\quad \left. + 4(p_\perp^2 b_y^2(1 - b_y^2) - 3p_\parallel p_\perp b_y^2(2 - b_y^2) + 3p_\parallel^2 b_y^4 - 3B_y^2 p_\parallel)\}^{\frac{1}{2}} \right]^{\frac{1}{2}}, \\
 c_s &= \frac{1}{\sqrt{2\rho}} \left[|\mathbf{B}|^2 + 2p_\perp + b_y^2(2p_\parallel - p_\perp) - \{(|\mathbf{B}|^2 + 2p_\perp + b_y^2(2p_\parallel - p_\perp))^2 \right. \\
 &\quad \left. + 4(p_\perp^2 b_y^2(1 - b_y^2) - 3p_\parallel p_\perp b_y^2(2 - b_y^2) + 3p_\parallel^2 b_y^4 - 3B_y^2 p_\parallel)\}^{\frac{1}{2}} \right]^{\frac{1}{2}}.
 \end{aligned}$$

B. Matrices for the Non-Conservative Terms

The matrix $\mathbf{C}_x(\mathbf{U})$ is given by,

$$\begin{pmatrix}
 0 & 0 & 0 & 0 & 0 & 0 & 0 & 0 & 0 & 0 & 0 \\
 -\frac{b_x^2|\mathbf{v}|^2}{2} & b_x^2 v_x & b_x^2 v_y & b_x^2 v_z & \frac{3}{2}b_x^2 & -b_x^2 & b_x^2 B_x + \frac{2\Gamma_x b_x}{|\mathbf{B}|} & b_x^2 B_y - \frac{2\Delta P b_{yxx}}{|\mathbf{B}|} & b_x^2 B_z - \frac{2\Delta P b_{zxx}}{|\mathbf{B}|} & b_x^2 \Psi & b_x^2 \Psi \\
 -\frac{b_x b_y |\mathbf{v}|^2}{2} & b_x b_y v_x & b_x b_y v_y & b_x b_y v_z & \frac{3}{2}b_x b_y & -b_x b_y & b_x b_y B_x + \frac{\Gamma_x b_y - \Delta P b_{yxx}}{|\mathbf{B}|} & b_x b_y B_y + \frac{\Gamma_y b_x - \Delta P b_{xyy}}{|\mathbf{B}|} & b_x b_y B_z - \frac{2\Delta P b_{xyz}}{|\mathbf{B}|} & b_x b_y \Psi & b_x b_y \Psi \\
 -\frac{b_x b_z |\mathbf{v}|^2}{2} & b_x b_z v_x & b_x b_z v_y & b_x b_z v_z & \frac{3}{2}b_x b_z & -b_x b_z & b_x b_z B_x + \frac{\Gamma_x b_z - \Delta P b_{zxx}}{|\mathbf{B}|} & b_x b_z B_y - \frac{2\Delta P b_{xyz}}{|\mathbf{B}|} & b_x b_z B_z + \frac{\Gamma_z b_x - \Delta P b_{xzz}}{|\mathbf{B}|} & b_x b_z \Psi & b_x b_z \Psi \\
 -\frac{2p_\parallel b_x (\mathbf{b} \cdot \mathbf{v})}{\rho} & \frac{2p_\parallel b_x b_x}{\rho} & \frac{2p_\parallel b_x b_y}{\rho} & \frac{2p_\parallel b_x b_z}{\rho} & 0 & 0 & 0 & 0 & 0 & 0 & 0 \\
 \Upsilon_1^x & \Upsilon_2^x & \Upsilon_3^x & \Upsilon_4^x & \frac{3}{2}b_x (\mathbf{b} \cdot \mathbf{v}) & -b_x (\mathbf{b} \cdot \mathbf{v}) & b_x (\mathbf{b} \cdot \mathbf{v}) B_x + \Theta_1^x & b_x (\mathbf{b} \cdot \mathbf{v}) B_y + \Theta_2^x & b_x (\mathbf{b} \cdot \mathbf{v}) B_z + \Theta_3^x & b_x (\mathbf{b} \cdot \mathbf{v}) \Psi & b_x (\mathbf{b} \cdot \mathbf{v}) \Psi \\
 0 & 0 & 0 & 0 & 0 & 0 & 0 & 0 & 0 & 0 & 0 \\
 0 & 0 & 0 & 0 & 0 & 0 & 0 & 0 & 0 & 0 & 0 \\
 0 & 0 & 0 & 0 & 0 & 0 & 0 & 0 & 0 & 0 & 0 \\
 0 & 0 & 0 & 0 & 0 & 0 & 0 & 0 & 0 & 0 & 0
 \end{pmatrix}$$

and matrix $\mathbf{C}_y(\mathbf{U})$ is given as,

$$\begin{pmatrix}
 0 & 0 & 0 & 0 & 0 & 0 & 0 & 0 & 0 & 0 & 0 \\
 -\frac{b_x b_y |\mathbf{v}|^2}{2} & b_x b_y v_x & b_x b_y v_y & b_x b_y v_z & \frac{3}{2}b_x b_y & -b_x b_y & b_x b_y B_x + \frac{\Gamma_x b_y - \Delta P b_{yxx}}{|\mathbf{B}|} & b_x b_y B_y + \frac{\Gamma_y b_x - \Delta P b_{xyy}}{|\mathbf{B}|} & b_x b_y B_z - \frac{2\Delta P b_{xyz}}{|\mathbf{B}|} & b_x b_y \Psi & b_x b_y \Psi \\
 -\frac{b_y^2 |\mathbf{v}|^2}{2} & b_y^2 v_x & b_y^2 v_y & b_y^2 v_z & \frac{3}{2}b_y^2 & -b_y^2 & b_y^2 B_x - \frac{2\Delta P b_{xyy}}{|\mathbf{B}|} & b_y^2 B_y + \frac{2\Gamma_y b_y}{|\mathbf{B}|} & b_y^2 B_z - \frac{2\Delta P b_{zyy}}{|\mathbf{B}|} & b_y^2 \Psi & b_y^2 \Psi \\
 -\frac{b_y b_z |\mathbf{v}|^2}{2} & b_y b_z v_x & b_y b_z v_y & b_y b_z v_z & \frac{3}{2}b_y b_z & -b_y b_z & b_y b_z B_x - \frac{2\Delta P b_{xyz}}{|\mathbf{B}|} & b_y b_z B_y + \frac{\Gamma_y b_z - \Delta P b_{zyy}}{|\mathbf{B}|} & b_y b_z B_z + \frac{\Gamma_z b_y - \Delta P b_{yzz}}{|\mathbf{B}|} & b_y b_z \Psi & b_y b_z \Psi \\
 -\frac{2p_\parallel b_y (\mathbf{b} \cdot \mathbf{v})}{\rho} & \frac{2p_\parallel b_y b_x}{\rho} & \frac{2p_\parallel b_y b_y}{\rho} & \frac{2p_\parallel b_y b_z}{\rho} & 0 & 0 & 0 & 0 & 0 & 0 & 0 \\
 \Upsilon_1^y & \Upsilon_2^y & \Upsilon_3^y & \Upsilon_4^y & \frac{3}{2}b_y (\mathbf{b} \cdot \mathbf{v}) & -b_y (\mathbf{b} \cdot \mathbf{v}) & b_y (\mathbf{b} \cdot \mathbf{v}) B_x + \Theta_1^y & b_y (\mathbf{b} \cdot \mathbf{v}) B_y + \Theta_2^y & b_y (\mathbf{b} \cdot \mathbf{v}) B_z + \Theta_3^y & b_y (\mathbf{b} \cdot \mathbf{v}) \Psi & b_y (\mathbf{b} \cdot \mathbf{v}) \Psi \\
 0 & 0 & 0 & 0 & 0 & 0 & 0 & 0 & 0 & 0 & 0 \\
 0 & 0 & 0 & 0 & 0 & 0 & 0 & 0 & 0 & 0 & 0 \\
 0 & 0 & 0 & 0 & 0 & 0 & 0 & 0 & 0 & 0 & 0
 \end{pmatrix}$$

where,

$$\Delta P = (p_\parallel - p_\perp), \Gamma_i = \Delta P(1 - b_i^2), \forall i \in \{x, y, z\}, b_{lmn} = b_l b_m b_n, \forall l, m, n \in \{x, y, z\}$$

$$\begin{aligned}
 \Theta_1^x &= \{(\mathbf{b} \cdot \mathbf{v}) + b_x v_x\} \left(\frac{\Gamma_x}{|\mathbf{B}|} \right) - \Delta P \frac{b_x^2 b_y v_y}{|\mathbf{B}|} - \Delta P \frac{b_x^2 b_z v_z}{|\mathbf{B}|}, \quad \Theta_2^x = \Gamma_y \left(\frac{b_x v_y}{|\mathbf{B}|} \right) - \Delta P \frac{b_x b_y b_z v_z}{|\mathbf{B}|} - \{(\mathbf{b} \cdot \mathbf{v}) + b_x v_x\} \frac{\Delta P b_x b_y}{|\mathbf{B}|}, \\
 \Theta_3^x &= \Gamma_z \left(\frac{b_x v_z}{|\mathbf{B}|} \right) - \Delta P \frac{b_x b_y b_z v_y}{|\mathbf{B}|} - \{(\mathbf{b} \cdot \mathbf{v}) + b_x v_x\} \frac{\Delta P b_x b_z}{|\mathbf{B}|}, \quad \Theta_1^y = \Gamma_x \left(\frac{b_y v_x}{|\mathbf{B}|} \right) - \Delta P \frac{b_x b_y b_z v_z}{|\mathbf{B}|} - \{(\mathbf{b} \cdot \mathbf{v}) + b_y v_y\} \frac{\Delta P b_x b_y}{|\mathbf{B}|}, \\
 \Theta_2^y &= \{(\mathbf{b} \cdot \mathbf{v}) + b_y v_y\} \left(\frac{\Gamma_y}{|\mathbf{B}|} \right) - \Delta P \frac{b_x^2 b_x v_x}{|\mathbf{B}|} - \Delta P \frac{b_x^2 b_z v_z}{|\mathbf{B}|}, \quad \Theta_3^y = \Gamma_z \left(\frac{b_y v_z}{|\mathbf{B}|} \right) - \Delta P \frac{b_x b_y b_z v_x}{|\mathbf{B}|} - \{(\mathbf{b} \cdot \mathbf{v}) + b_y v_y\} \frac{\Delta P b_y b_z}{|\mathbf{B}|}, \\
 \Upsilon_1^x &= -b_x (\mathbf{b} \cdot \mathbf{v}) \frac{|\mathbf{v}|^2}{2} - \frac{\Delta P b_x (\mathbf{b} \cdot \mathbf{v})}{\rho}, \quad \Upsilon_2^x = b_x (\mathbf{b} \cdot \mathbf{v}) v_x + \frac{\Delta P b_x^2}{\rho}, \quad \Upsilon_3^x = b_x (\mathbf{b} \cdot \mathbf{v}) v_y + \frac{\Delta P b_x b_y}{\rho}, \quad \Upsilon_4^x = b_x (\mathbf{b} \cdot \mathbf{v}) v_z + \frac{\Delta P b_x b_z}{\rho} \\
 \Upsilon_1^y &= -b_y (\mathbf{b} \cdot \mathbf{v}) \frac{|\mathbf{v}|^2}{2} - \frac{\Delta P b_y (\mathbf{b} \cdot \mathbf{v})}{\rho}, \quad \Upsilon_2^y = b_y (\mathbf{b} \cdot \mathbf{v}) v_x + \frac{\Delta P b_x b_y}{\rho}, \quad \Upsilon_3^y = b_y (\mathbf{b} \cdot \mathbf{v}) v_y + \frac{\Delta P b_y^2}{\rho} \text{ and } \Upsilon_4^y = b_y (\mathbf{b} \cdot \mathbf{v}) v_z + \frac{\Delta P b_y b_z}{\rho}.
 \end{aligned}$$

C. Entropy scaling of right eigenvectors

The eigenvectors for (29) are detailed in Section C.1. The entropy-scaled eigenvectors are derived in Section C.2. We perform all of the analysis using primitive variables $\mathbf{w} = \{\rho, v_x, v_y, v_z, p_{\parallel}, p_{\perp}, B_x, B_y, B_z, \Psi\}$.

C.1. Right eigenvectors

The right eigenvectors for the primitive formulation of the system (29) with respect to the primitive variables \mathbf{w} in x -direction for the eigenvalues K_x (define in Section 3.3) are given as follows:

$$\begin{aligned}
 R_{v_x}^1 &= \begin{pmatrix} 1 \\ 0 \\ 0 \\ 0 \\ 0 \\ 0 \\ 0 \\ 0 \\ 0 \\ 0 \end{pmatrix}, \quad R_{v_x}^2 = \begin{pmatrix} 0 \\ 0 \\ 0 \\ 0 \\ 1 \\ 0 \\ 0 \\ 0 \\ 0 \\ 0 \end{pmatrix}, \quad R_{v_x \pm c_h} = \begin{pmatrix} 0 \\ 0 \\ 0 \\ 0 \\ 0 \\ 0 \\ \pm 1 \\ 0 \\ 0 \\ 1 \end{pmatrix}, \quad R_{v_x \pm v_{ax}} = \begin{pmatrix} 0 \\ 0 \\ \pm \beta_z \\ \mp \beta_y \\ 0 \\ 0 \\ 0 \\ 0 \\ -\beta_z \operatorname{sgn}(B_x) \sqrt{\rho} \\ \beta_y \operatorname{sgn}(B_x) \sqrt{\rho} \\ 0 \end{pmatrix}, \\
 R_{v_x \pm c_f} &= \begin{pmatrix} \alpha_f \rho \\ \pm \alpha_f c_f \\ \mp \alpha_s c_s \beta_y \operatorname{sgn}(B_x) \\ \mp \alpha_s c_s \beta_z \operatorname{sgn}(B_x) \\ \alpha_f p_{\parallel} \\ \alpha_f \rho a^2 \\ 0 \\ \alpha_s a \beta_y \sqrt{\rho} \\ \alpha_s a \beta_z \sqrt{\rho} \\ 0 \end{pmatrix}, \quad R_{v_x \pm c_s} = \begin{pmatrix} \alpha_s \rho \\ \pm \alpha_s c_s \\ \pm \alpha_f c_f \beta_y \operatorname{sgn}(B_x) \\ \pm \alpha_f c_f \beta_z \operatorname{sgn}(B_x) \\ \alpha_s p_{\parallel} \\ \alpha_s \rho a^2 \\ 0 \\ -\alpha_f a \beta_y \sqrt{\rho} \\ -\alpha_f a \beta_z \sqrt{\rho} \\ 0 \end{pmatrix},
 \end{aligned}$$

where,

$$\begin{aligned}
 v_{ax}^2 &= \frac{B_x^2}{\rho}, \quad v_a^2 = \frac{|\mathbf{B}|^2}{\rho}, \quad a^2 = \frac{2P_{\perp}}{\rho}, \\
 c_{f,s}^2 &= \frac{1}{2} \left[(v_a^2 + a^2) \pm \sqrt{(v_a^2 + a^2)^2 - 4v_{ax}^2 a^2} \right], \\
 \alpha_f^2 &= \frac{a^2 - c_s^2}{c_f^2 - c_s^2}, \quad \alpha_s^2 = \frac{c_f^2 - a^2}{c_f^2 - c_s^2}, \quad \beta_y = \frac{B_y}{\sqrt{B_y^2 + B_z^2}}, \quad \beta_z = \frac{B_z}{\sqrt{B_y^2 + B_z^2}}.
 \end{aligned}$$

Similarly, for the y -direction, eigenvectors corresponding to the eigenvalues K_y (define in Section 3.3) are given below:

$$R_{v_y}^1 = \begin{pmatrix} 1 \\ 0 \\ 0 \\ 0 \\ 0 \\ 0 \\ 0 \\ 0 \\ 0 \end{pmatrix}, R_{v_y}^2 = \begin{pmatrix} 0 \\ 0 \\ 0 \\ 0 \\ 1 \\ 0 \\ 0 \\ 0 \\ 0 \end{pmatrix}, R_{v_y \pm c_h} = \begin{pmatrix} 0 \\ 0 \\ 0 \\ 0 \\ 0 \\ 0 \\ 0 \\ \pm 1 \\ 0 \\ 1 \end{pmatrix}, R_{v_y \pm v_{ay}} = \begin{pmatrix} 0 \\ \pm \beta_z \\ 0 \\ \mp \beta_x \\ 0 \\ 0 \\ -\beta_z \operatorname{sgn}(B_y) \sqrt{\rho} \\ 0 \\ \beta_x \operatorname{sgn}(B_y) \sqrt{\rho} \\ 0 \end{pmatrix},$$

$$R_{v_y \pm c_f} = \begin{pmatrix} \alpha_f \rho \\ \mp \alpha_s c_s \beta_x \operatorname{sgn}(B_y) \\ \pm \alpha_f c_f \\ \mp \alpha_s c_s \beta_z \operatorname{sgn}(B_y) \\ \alpha_f p_{\parallel} \\ \alpha_f \rho a^2 \\ \alpha_s a \beta_x \sqrt{\rho} \\ 0 \\ \alpha_s a \beta_z \sqrt{\rho} \\ 0 \end{pmatrix}, R_{v_y \pm c_s} = \begin{pmatrix} \alpha_s \rho \\ \pm \alpha_f c_f \beta_x \operatorname{sgn}(B_y) \\ \pm \alpha_s c_s \\ \pm \alpha_f c_f \beta_z \operatorname{sgn}(B_y) \\ \alpha_s p_{\parallel} \\ \alpha_s \rho a^2 \\ -\alpha_f a \beta_x \sqrt{\rho} \\ 0 \\ -\alpha_f a \beta_z \sqrt{\rho} \\ 0 \end{pmatrix},$$

where,

$$v_{ay}^2 = \frac{B_y^2}{\rho}, v_a^2 = \frac{|\mathbf{B}|^2}{\rho}, a^2 = \frac{2P_{\perp}}{\rho},$$

$$c_{f,s}^2 = \frac{1}{2} \left[(v_a^2 + a^2) \pm \sqrt{(v_a^2 + a^2)^2 - 4v_{ay}^2 a^2} \right].$$

$$\alpha_f^2 = \frac{a^2 - c_s^2}{c_f^2 - c_s^2}, \alpha_s^2 = \frac{c_f^2 - a^2}{c_f^2 - c_s^2}, \beta_x = \frac{B_x}{\sqrt{B_x^2 + B_z^2}}, \beta_z = \frac{B_z}{\sqrt{B_x^2 + B_z^2}}.$$

The set of eigenvectors in both directions is linearly independent.

C.2. Entropy-scaled right eigenvectors via Barth scaling process

Here we will follow the Barth scaling process [68] and calculate the entropy-scaled right eigenvectors for x -direction. For the system (29), let R^x be the right eigenvector matrix for the system (29) in terms of conservative variables and R_w^x be right eigenvectors in terms of the primitive variables described in C.1. Then we have

$$R^x = \frac{\partial \mathbf{U}}{\partial \mathbf{w}} R_w^x$$

where, $\frac{\partial \mathbf{U}}{\partial \mathbf{w}}$ is the Jacobian matrix for the change of variable, given by

$$\frac{\partial \mathbf{U}}{\partial \mathbf{w}} = \begin{pmatrix} 1 & 0 & 0 & 0 & 0 & 0 & 0 & 0 & 0 & 0 \\ v_x & \rho & 0 & 0 & 0 & 0 & 0 & 0 & 0 & 0 \\ v_y & 0 & \rho & 0 & 0 & 0 & 0 & 0 & 0 & 0 \\ v_z & 0 & 0 & \rho & 0 & 0 & 0 & 0 & 0 & 0 \\ 0 & 0 & 0 & 0 & 1 & 0 & 0 & 0 & 0 & 0 \\ \frac{v^2}{2} & \rho v_x & \rho v_y & \rho v_z & \frac{1}{2} & 1 & B_x & B_y & B_z & \Psi \\ 0 & 0 & 0 & 0 & 0 & 0 & 1 & 0 & 0 & 0 \\ 0 & 0 & 0 & 0 & 0 & 0 & 0 & 1 & 0 & 0 \\ 0 & 0 & 0 & 0 & 0 & 0 & 0 & 0 & 1 & 0 \\ 0 & 0 & 0 & 0 & 0 & 0 & 0 & 0 & 0 & 1 \end{pmatrix}.$$

and the matrix $R_{\mathbf{w}}^x$ is the right eigenvector matrix for the system (29) in terms of primitive variable (see C.1), which is given below,

$$R_{\mathbf{w}}^x = \left(R_{v_x - c_f} \quad R_{v_x - c_s} \quad R_{v_x - c_h} \quad R_{v_x - v_{ax}} \quad R_{v_x}^1 \quad R_{v_x}^2 \quad R_{v_x + v_{ax}} \quad R_{v_x + c_h} \quad R_{v_x + c_s} \quad R_{v_x + c_f} \right).$$

Our aim is to find the scaling matrix T^x such that the scaled right eigenvector matrix $\tilde{R}^x = R^x T^x$ satisfies

$$\frac{\partial \mathbf{U}}{\partial \mathbf{V}} = \tilde{R}^x \tilde{R}^{x\top} \quad (49)$$

where \mathbf{V} is the entropy variable vector as in (8). Now we follow [68] and define the matrix

$$\mathcal{Y}^x = (R_{\mathbf{w}}^x)^{-1} \frac{\partial \mathbf{w}}{\partial \mathbf{V}} \left(\frac{\partial \mathbf{U}}{\partial \mathbf{w}_x} \right)^{-\top} (R_{\mathbf{w}}^x)^{-\top}$$

After doing some calculations, we get

$$\mathcal{Y}^x = \begin{pmatrix} \frac{1}{8\rho} & 0 & 0 & 0 & 0 & 0 & 0 & 0 & 0 & 0 \\ 0 & \frac{1}{8\rho} & 0 & 0 & 0 & 0 & 0 & 0 & 0 & 0 \\ 0 & 0 & \frac{p_{\perp}}{4\rho} & 0 & 0 & 0 & 0 & 0 & 0 & 0 \\ 0 & 0 & 0 & \frac{p_{\perp}}{4\rho^2} & 0 & 0 & 0 & 0 & 0 & 0 \\ 0 & 0 & 0 & 0 & \frac{p}{4} & \frac{p_{\parallel}}{4} & 0 & 0 & 0 & 0 \\ 0 & 0 & 0 & 0 & \frac{p_{\parallel}}{4} & \frac{5p_{\parallel}^2}{4\rho} & 0 & 0 & 0 & 0 \\ 0 & 0 & 0 & 0 & 0 & 0 & \frac{p_{\perp}}{4\rho^2} & 0 & 0 & 0 \\ 0 & 0 & 0 & 0 & 0 & 0 & 0 & \frac{p_{\perp}}{4\rho} & 0 & 0 \\ 0 & 0 & 0 & 0 & 0 & 0 & 0 & 0 & \frac{1}{8\rho} & 0 \\ 0 & 0 & 0 & 0 & 0 & 0 & 0 & 0 & 0 & \frac{1}{8\rho} \end{pmatrix}.$$

Then the scaling matrix T^x is the square root of \mathcal{Y}^x is given below

$$\begin{pmatrix} \frac{1}{2\sqrt{2\rho}} & 0 & 0 & 0 & 0 & 0 & 0 & 0 & 0 & 0 \\ 0 & \frac{1}{2\sqrt{2\rho}} & 0 & 0 & 0 & 0 & 0 & 0 & 0 & 0 \\ 0 & 0 & \frac{\sqrt{p_\perp}}{2\sqrt{\rho}} & 0 & 0 & 0 & 0 & 0 & 0 & 0 \\ 0 & 0 & 0 & \frac{\sqrt{p_\perp}}{2\rho} & 0 & 0 & 0 & 0 & 0 & 0 \\ 0 & 0 & 0 & 0 & \frac{\sqrt{\rho(2p_\parallel+\rho)}}{2\sqrt{5p_\parallel^2+4p_\parallel\rho+\rho^2}} & \frac{p_\parallel\sqrt{\rho}}{2\sqrt{5p_\parallel^2+4p_\parallel\rho+\rho^2}} & 0 & 0 & 0 & 0 \\ 0 & 0 & 0 & 0 & \frac{p_\parallel\sqrt{\rho}}{2\sqrt{5p_\parallel^2+4p_\parallel\rho+\rho^2}} & \frac{p_\parallel(5p_\parallel+2\rho)}{2\sqrt{\rho(5p_\parallel^2+4p_\parallel\rho+\rho^2)}} & 0 & 0 & 0 & 0 \\ 0 & 0 & 0 & 0 & 0 & 0 & \frac{\sqrt{p_\perp}}{2\rho} & 0 & 0 & 0 \\ 0 & 0 & 0 & 0 & 0 & 0 & 0 & \frac{\sqrt{p_\perp}}{2\sqrt{\rho}} & 0 & 0 \\ 0 & 0 & 0 & 0 & 0 & 0 & 0 & 0 & \frac{1}{2\sqrt{2\rho}} & 0 \\ 0 & 0 & 0 & 0 & 0 & 0 & 0 & 0 & 0 & \frac{1}{2\sqrt{2\rho}} \end{pmatrix}.$$

In a similar manner, for the y -direction, we obtain the scaling matrix T^y . Combining all the discussions, in x -direction, the entropy-scaled right eigenvectors matrix in terms of primitive variables is given by,

$$\tilde{R}_w^x = R_w^x T^x$$

$$\tilde{R}_w^x = \left(\tilde{R}_{v_x-c_f} \quad \tilde{R}_{v_x-c_s} \quad \tilde{R}_{v_x-c_h} \quad \tilde{R}_{v_x-v_{ax}} \quad \tilde{R}_{v_x}^1 \quad \tilde{R}_{v_x}^2 \quad \tilde{R}_{v_x+v_{ax}} \quad \tilde{R}_{v_x+c_h} \quad \tilde{R}_{v_x+c_s} \quad \tilde{R}_{v_x+c_f} \right).$$

where,

$$\tilde{R}_{v_x}^1 = \begin{pmatrix} \frac{\sqrt{\rho(2p_\parallel+\rho)}}{2\sqrt{5p_\parallel^2+4p_\parallel\rho+\rho^2}} \\ 0 \\ 0 \\ 0 \\ 0 \\ \frac{p_\parallel\sqrt{\rho}}{2\sqrt{5p_\parallel^2+4p_\parallel\rho+\rho^2}} \\ 0 \\ 0 \\ 0 \\ 0 \\ 0 \end{pmatrix}, \quad \tilde{R}_{v_x}^2 = \begin{pmatrix} \frac{p_\parallel\sqrt{\rho}}{2\sqrt{5p_\parallel^2+4p_\parallel\rho+\rho^2}} \\ 0 \\ 0 \\ 0 \\ 0 \\ \frac{p_\parallel(5p_\parallel+2\rho)}{2\sqrt{\rho(5p_\parallel^2+4p_\parallel\rho+\rho^2)}} \\ 0 \\ 0 \\ 0 \\ 0 \\ 0 \end{pmatrix}, \quad \tilde{R}_{v_x\pm c_h} = \frac{1}{2} \begin{pmatrix} 0 \\ 0 \\ 0 \\ 0 \\ 0 \\ 0 \\ \pm\sqrt{\frac{p_\perp}{\rho}} \\ 0 \\ 0 \\ \sqrt{\frac{p_\perp}{\rho}} \end{pmatrix},$$

$$\tilde{R}_{v_x\pm v_{ax}} = \frac{1}{2} \begin{pmatrix} 0 \\ 0 \\ \pm\frac{\sqrt{p_\perp}}{\rho}\beta_z \\ \mp\frac{\sqrt{p_\perp}}{\rho}\beta_y \\ 0 \\ 0 \\ 0 \\ -\sqrt{\frac{p_\perp}{\rho}}\beta_z \\ \sqrt{\frac{p_\perp}{\rho}}\beta_y \\ 0 \end{pmatrix}, \quad \tilde{R}_{v_x\pm c_f} = \frac{1}{2\sqrt{2}} \begin{pmatrix} \alpha_f\sqrt{\rho} \\ \pm\frac{\alpha_f c_f}{\sqrt{\rho}} \\ \mp\frac{\alpha_s c_s \beta_y}{\sqrt{\rho}} \\ \mp\frac{\alpha_s c_s \beta_z}{\sqrt{\rho}} \\ \pm\frac{\alpha_f p_\parallel}{\sqrt{\rho}} \\ \alpha_f\sqrt{\rho a^2} \\ 0 \\ \alpha_s a \beta_y \\ \alpha_s a \beta_z \\ 0 \end{pmatrix}, \quad \tilde{R}_{v_x\pm c_s} = \frac{1}{2\sqrt{2}} \begin{pmatrix} \alpha_s\sqrt{\rho} \\ \pm\frac{\alpha_s c_s}{\sqrt{\rho}} \\ \pm\frac{\alpha_f c_f \beta_y}{\sqrt{\rho}} \\ \pm\frac{\alpha_f c_f \beta_z}{\sqrt{\rho}} \\ \alpha_s\frac{p_\parallel}{\sqrt{\rho}} \\ \alpha_s\sqrt{\rho a^2} \\ 0 \\ -\alpha_f a \beta_y \\ -\alpha_f a \beta_z \\ 0 \end{pmatrix}$$

Similarly, in the y -direction, the entropy-scaled right eigenvectors matrix in terms of primitive variables is given by,

$$\tilde{\mathbf{R}}^y_{\mathbf{w}} = \mathbf{R}^y_{\mathbf{w}} T^y$$

$$\tilde{\mathbf{R}}^y_{\mathbf{w}} = \left(\tilde{\mathbf{R}}_{v_y - c_f} \quad \tilde{\mathbf{R}}_{v_y - c_s} \quad \tilde{\mathbf{R}}_{v_y - c_h} \quad \tilde{\mathbf{R}}_{v_y - v_{ay}} \quad \tilde{\mathbf{R}}^1_{v_y} \quad \tilde{\mathbf{R}}^2_{v_y} \quad \tilde{\mathbf{R}}_{v_y + v_{ay}} \quad \tilde{\mathbf{R}}_{v_y + c_h} \quad \tilde{\mathbf{R}}_{v_y + c_s} \quad \tilde{\mathbf{R}}_{v_y + c_f} \right).$$

where,

$$\tilde{\mathbf{R}}^1_{v_y} = \begin{pmatrix} \frac{\sqrt{\rho}(2p_{\parallel} + \rho)}{2\sqrt{5p_{\parallel}^2 + 4p_{\parallel}\rho + \rho^2}} \\ 0 \\ 0 \\ 0 \\ 0 \\ \frac{p_{\parallel}\sqrt{\rho}}{2\sqrt{5p_{\parallel}^2 + 4p_{\parallel}\rho + \rho^2}} \\ 0 \\ 0 \\ 0 \\ 0 \\ 0 \\ 0 \end{pmatrix}, \quad \tilde{\mathbf{R}}^2_{v_y} = \begin{pmatrix} \frac{p_{\parallel}\sqrt{\rho}}{2\sqrt{5p_{\parallel}^2 + 4p_{\parallel}\rho + \rho^2}} \\ 0 \\ 0 \\ 0 \\ 0 \\ \frac{p_{\parallel}(5p_{\parallel} + 2\rho)}{2\sqrt{\rho(5p_{\parallel}^2 + 4p_{\parallel}\rho + \rho^2)}} \\ 0 \\ 0 \\ 0 \\ 0 \\ 0 \\ 0 \end{pmatrix}, \quad \tilde{\mathbf{R}}_{v_y \pm c_h} = \begin{pmatrix} 0 \\ 0 \\ 0 \\ 0 \\ 0 \\ 0 \\ 0 \\ \pm\sqrt{\frac{p_{\perp}}{\rho}} \\ 0 \\ \sqrt{\frac{p_{\perp}}{\rho}} \end{pmatrix},$$

$$\tilde{\mathbf{R}}_{v_y \pm v_{ay}} = \frac{1}{2} \begin{pmatrix} 0 \\ \pm\sqrt{\frac{p_{\perp}}{\rho}}\beta_z \\ 0 \\ \mp\sqrt{\frac{p_{\perp}}{\rho}}\beta_x \\ 0 \\ 0 \\ -\sqrt{\frac{p_{\perp}}{\rho}}\beta_z \\ 0 \\ \sqrt{\frac{p_{\perp}}{\rho}}\beta_x \\ 0 \end{pmatrix}, \quad \tilde{\mathbf{R}}_{v_y \pm c_f} = \frac{1}{2\sqrt{2}} \begin{pmatrix} \alpha_f\sqrt{\rho} \\ \mp\alpha_s c_s \beta_x \\ \pm\frac{\sqrt{\rho}}{\alpha_f c_f} \\ \mp\frac{\sqrt{\rho}}{\alpha_s c_s \beta_z} \\ \alpha_f \frac{p_{\parallel}}{\sqrt{\rho}} \\ \alpha_f \sqrt{\rho} a^2 \\ \alpha_s a \beta_x \\ 0 \\ \alpha_s a \beta_z \\ 0 \end{pmatrix}, \quad \tilde{\mathbf{R}}_{v_y \pm c_f} = \frac{1}{2\sqrt{2}} \begin{pmatrix} \alpha_s \sqrt{\rho} \\ \alpha_f c_f \beta_x \\ \pm\frac{\sqrt{\rho}}{\alpha_s c_s} \\ \pm\frac{\sqrt{\rho}}{\alpha_f c_f \beta_z} \\ \alpha_s \frac{p_{\parallel}}{\sqrt{\rho}} \\ \alpha_s \sqrt{\rho} a^2 \\ -\alpha_f a \beta_x \\ 0 \\ -\alpha_f a \beta_z \\ 0 \end{pmatrix},$$

All the notations are defined in C.1.

D. Central Difference formulas for derivatives in non-conservative terms

For a grid function $a_{i,j}$, the second-order central difference approximations to approximate the derivatives $\left(\frac{\partial a}{\partial x}\right)_{i,j}$ and $\left(\frac{\partial a}{\partial y}\right)_{i,j}$ in x and y -directions are given by,

$$\left(\frac{\partial a}{\partial x}\right)_{i,j} = \frac{a_{i+1,j} - a_{i-1,j}}{2\Delta x} \quad \text{and} \quad \left(\frac{\partial a}{\partial y}\right)_{i,j} = \frac{a_{i,j+1} - a_{i,j-1}}{2\Delta y}.$$

Similarly, the fourth-order central difference approximations to approximate the derivatives $\left(\frac{\partial a}{\partial x}\right)_{i,j}$ and $\left(\frac{\partial a}{\partial y}\right)_{i,j}$ in x and y -directions are given below

$$\left(\frac{\partial a}{\partial x}\right)_{i,j} = \frac{-a_{i+2,j} + 8a_{i+1,j} - 8a_{i-1,j} + a_{i-2,j}}{12\Delta x},$$

and

$$\left(\frac{\partial a}{\partial y}\right)_{i,j} = \frac{-a_{i,j+2} + 8a_{i,j+1} - 8a_{i,j-1} + a_{i,j-2}}{12\Delta y}.$$